Optimized Modulation Strategy of NH3L-DAB Converter to Minimize RMS Current for Wide Voltage Range Applications

Ze Zhang, Lijun Hang, *Senior Member, IEEE*, Anping Tong, *Student Member, IEEE*, Kejian Chen, Zhenyuan Ou, Yuanbin He, *Member, IEEE*, Zhen He, *Member, IEEE*, Pingliang Zeng, *Senior Member, IEEE*, Qiuwei Wu, *Senior Member, IEEE*, and Guojie Li, *Senior Member, IEEE*

***Abstract*—Dual active bridge (DAB) converter is one of the most popular bidirectional isolated dc/dc converters. Comparing with the two-level DAB converter, the multilevel DAB topologies take advantages of providing more control degrees of freedom to enhance the control flexibility. Therefore, these topologies are promising alternatives for wide voltage range applications. This article proposed an optimizing modulation strategy for neutral-point-clamped hybrid three-level dual active bridge (NH3L-DAB) converter to minimize the rms value of inductor current and the conduction losses. First, the basic operating principle of NH3L-DAB is analyzed comprehensively in the article. Afterward, the concept of global optimal condition is employed to derive the optimal modulation, and the corresponding analytical expressions of the control coordinates for rms current minimization are derived. By applying the optimal modulation strategy, NH3L-DAB facilitates to break the performance barriers of the prior-of-art of two-level DAB converter when the voltage transmission ratio has large variation. Finally, a bidirectional prototype with 200–450 V input and 20–28.8 V output is built to demonstrate the superior performance of the proposed optimal modulation strategy, and the detailed explanation of the experimental results is given as well.**

***Index Terms*—Optimized modulation method, soft switching, three-level dual active bridge (DAB) converter, wide voltage range applications.**

I. INTRODUCTION

THE isolated dc/dc power converters with wide input/output voltage range and high power density now continuously attract interests in various applications, such as data center power supplies, dc/dc converters for automotive applications, battery chargers, and power converters for solar system or fuel cell [1]–[8]. Some promising topologies have been extensively discussed in the literature. Among them, the dual active bridge (DAB) converter [9] is a perspective topology by taking advantages of the low number passive components, control flexibility, and soft-switching capabilities.

Assuming that the turns ratio of a high-frequency transformer of the isolated power converter is N, and M is referred to the voltage transmission ratio, where $M = N \times V_{\text{out}}/V_{\text{in}}$. γ is defined to represent the normalized voltage conversion range, i.e., $\gamma = \frac{V_{in\_\max}}{V_{\text{in\_min}}} \times \frac{V_{\text{out\_max}}}{V_{\text{out\_min}}}$. Therefore, the voltage operating range will expand when γ increases. And γ also equals to $M_{\max}/M_{\min}$. The applications with $\gamma \geq 2$ can be basically regarded as the wide voltage range applications [10], [11].

It is known that the conventional two-level DAB (2L-DAB) converter has the highest efficiency around $M = 1$ [12], [13]. In order to improve the converter performance when $M \neq 1$ in practical implementation, a lot of literature introduced advanced modulation schemes [5], [14]–[21], in which some or all available control variables of 2L-DAB converter are adjusted based on specific functions (e.g., current stress, efficiency, or conduction losses). However, there are performance barriers of 2L-DAB converter, and the efficiency or other performances of the circuit are hard to be further improved. Such performance barriers are addressed in detail in Section III.

The multilevel converters, which are single-stage architecture, can be regarded as a strong competitor for wide voltage application. The single-stage solution takes advantages of the elimination of the bulky capacitor on the intermediate dc bus; therefore, it facilitates to achieve higher power density [46]. The multilevel DAB converters have been presented in the literature [13], [22]–[38]. The operation principle and modulations of three-level DAB converter with only one three-level half-bridge in the primary side or secondary side [28], [39], [41] are similar to that of 2L-DAB converter with half input or output voltage as the three-level half-bridge can only provide 0 and $\pm v_{\text{dc}}/2$ voltage levels, wherein v_{dc} represents the input or output dc voltage of DAB converter. The work in [27], [32], and [33] focused on the modulation optimization and soft-switching characteristics

---

Manuscript received May 14, 2021; revised August 16, 2021, October 29, 2021, and December 27, 2021; accepted January 22, 2022. Date of publication February 4, 2022; date of current version March 24, 2022. This work was supported in part by the National Natural Science Foundation of China under Grant 51777049 and in part by the Pioneer and "Leading Goose" R&D Program of Zhejiang under Grant 2022C01059. Recommended for publication by Associate Editor M. Chen. *(Corresponding author: Lijun Hang.)*

Ze Zhang, Lijun Hang, Kejian Chen, Zhenyuan Ou, Yuanbin He, Zhen He, and Pingliang Zeng are with the Regional Energy Internet Technology Zhejiang Engineering Laboratory, School of Automation, Hangzhou Dianzi University, Hangzhou 310018, China (e-mail: zhangze@hdu.edu.cn; lijunhang.hhy@aliyun.com; 19061310@hdu.edu.cn; 1075029260@qq.com; yuanbinhe@hdu.edu.cn; hezhen_hz@hust.edu.cn; plzeng@hotmail.com).

Anping Tong and Guojie Li are with the Shanghai Jiao Tong University, Shanghai 200240, China (e-mail: tonganping@huawei.com; liguojie@sjtu.edu.cn).

Qiuwei Wu is with the Tsinghua-Berkeley Shenzhen Institute, Shenzhen 518000, China (e-mail: qiuwu@sz.tsinghua.edu.cn).

Color versions of one or more figures in this article are available at https://doi.org/10.1109/TPEL.2022.3148248.

Digital Object Identifier 10.1109/TPEL.2022.3148248

of the neutral-point-clamped (NPC) three-level DAB converter with symmetric topology, in which both of primary side and secondary side are three-level full bridge. However, extra eight switching devices are needed.

The asymmetric three-level DAB converter, which consists of one three-level full bridge and one two-level full bridge, has been discussed in [12], [25], and [26]. In [12], the optimized modulation method to minimize rms value of inductor current has been investigated; however, the numeric solutions rather than analytical expressions are given. In [30], a block capacitor is series connected with the high-frequency transformer to further reduce the transformer rms current and to enlarge the soft-switching range. Furthermore, the hybrid three-level DAB converters are investigated in [13], [29], [30], and [38]. The hybrid three-level architecture indicates that the primary full bridge or the secondary full bridge of DAB converter is composed by a two-level half-bridge and a three-level half-bridge. Comparing with the 2L-DAB converter, the hybrid three-level DAB converters need only one [30] or two [29] additional active switching devices, in contrast, the asymmetric three-level DAB [12], [30] needs four additional active switching devices. In addition, the benefit of lower withstand voltage switching devices can be used in the three-level bridge arm, and both cost and efficiency can be improved. Hence, the hybrid three-level architecture takes advantages of low complexity and cost-efficiency.

In [13], the voltage matching control has been presented. That modulation method has concise and analytical expressions, and it is very convenient for practical use. However, only the operating conditions with $M\in[1/2, 1]$ (i.e., $v_1/2 < v_2 \times N < v_1$) are mainly discussed in [13], and such modulation strategy can be improved further to minimize rms current.

In this article, the DAB converter with hybrid three-level primary side is investigated, in which one of the two-level half-bridge of conventional 2L-DAB has been replaced by the NPC three-level half-bridge. Hence, the ac voltage of the primary side has an extra voltage level of $\pm v_1/2$, and the duty ratio of all levels is adjustable. And this hybrid three-level DAB converter has four control degrees, which can shape the inductor current more flexibly. However, it is considerably complicated to optimize the modulation methods. In the prior-of-art research, the optimization of modulations is mainly based on the numeric method [12], [33]. In order to solve the optimization problem, the concept of global optimal condition (GOC) in [19] is proposed for hybrid three-level DAB converter. Afterward, the optimal modulation schemes to minimize the rms value of inductor current are derived in analytical forms, which facilitates the proposed modulation method to be implemented in a digital controller in real time.

The rest of this article is organized as follows. The operating principles and steady-state characteristics of hybrid three-level DAB converter are illustrated in Section II. In Section III, the performance barriers of the conventional 2L-DAB converter are discussed to illustrate the potential of three-level DAB converter. Subsequently, in Section IV, the optimal modulation methods with respect to minimum rms value of inductor current are derived for three different ranges of voltage ratio, $0 \leq M \leq 0.5$, $0.5 < M \leq 1$, and $1 < M$ in forward power flow mode. In Section V, the optimal modulation methods with respect to minimum rms value of inductor current in reverse power flow mode are derived for three different ranges of voltage ratio, $0 \leq M < 1$, $1 \leq M \leq 2$, and $2 < M$. Moreover, the performance improvements of the three-level DAB converter with the proposed modulation strategies also have been illustrated. In Section VI, the experimental results are given to verify the effectiveness of the proposed solution for wide voltage range applications. The detailed explanation of the experimental results is given as well. Finally, Section VII concludes this article.

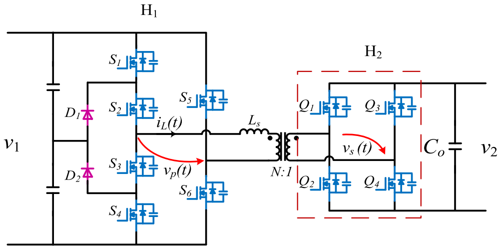

Fig. 1. Circuit topology of hybrid NPC three-level DAB converter in power forward flow mode.

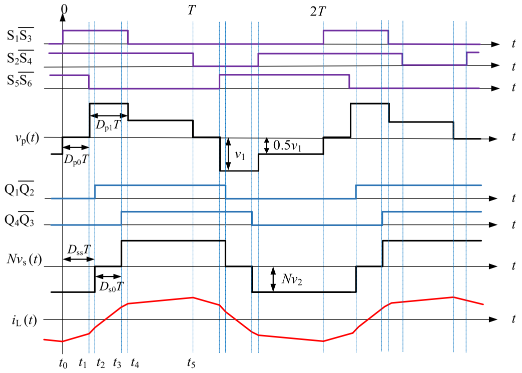

Fig. 2. Typical operating waveforms of NH3L-DAB converter.

II. OPERATING PRINCIPLE OF NEUTRAL-POINT-CLAMPED HYBRID THREE-LEVEL DAB (NH3L-DAB) CONVERTER

A. *Basic Operating Principle for the NH3L-DAB Converter in Forward Mode*

Fig. 1 shows the circuit configuration of the NH3L-DAB converter, which consists of two full bridges: H_1 and H_2. It should be clarified that when the power is transferred from v_1 to v_2, it is called forward mode, and vice versa. The ac voltage of H_1 and H_2 is denoted by $v_\mathrm{p}(t)$ and $v_\mathrm{s}(t)$, respectively. In contrast with the conventional 2L-DAB converter, H_1 of the NH3L-DAB converter has a diode clamped three-level bridge leg, which can generate three kinds of voltage levels for $v_\mathrm{p}(t)$: 0, $\pm v_1/2$, and $\pm v_1$. H_1 and H_2 are connected by a high-frequency transformer and an ac inductor L_s. $i_L(t)$ is the current of L_s. By taking advantages of the additional intermediate voltage level, NH3L-DAB is more flexible to shape the inductor current $i_L(t)$.

The typical operating waveforms of NH3L-DAB converter are illustrated in Fig. 2. There are four control degrees when the power flow is from port v_1 to v_2, i.e., D_p0, D_p1, D_ss, and

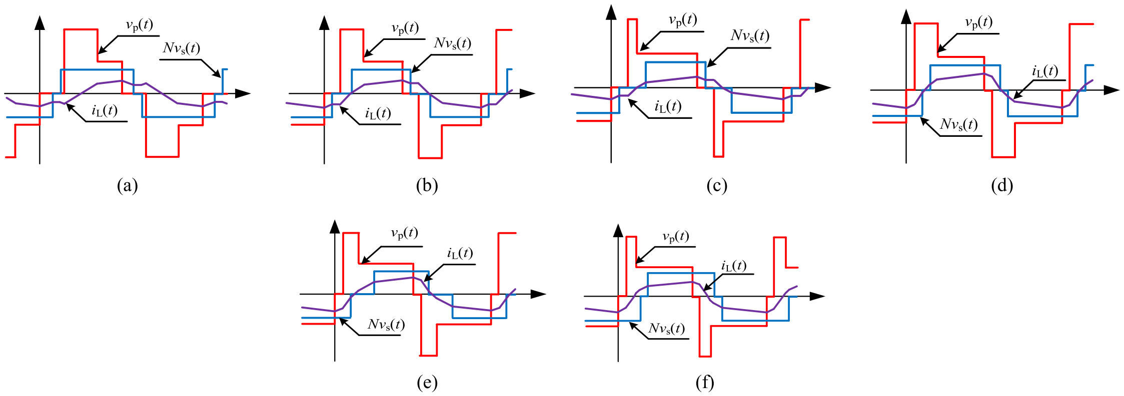

Fig. 3. Operating waveforms of Modes 1–6. (a) Mode 1. (b) Mode 2. (c) Mode 3. (d) Mode 4. (e) Mode 5. (f) Mode 6.

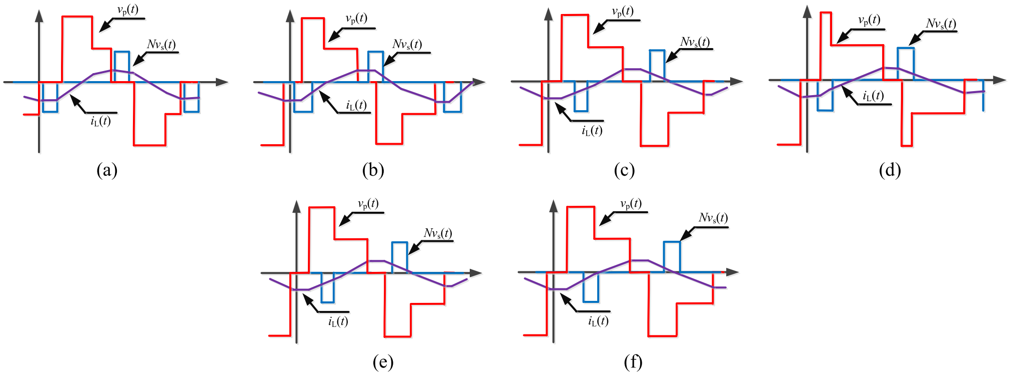

Fig. 4. Operating waveforms of six uncommon operating modes. (a) Mode 7. (b) Mode 8. (c) Mode 9. (d) Mode 10. (e) Mode 11. (f) Mode 12.

TABLE I
SWITCHING MOMENT FOR EACH SWITCHING DEVICE IN FORWARD MODE

Switching Devices	Switching Moment
S_1/S_3	$0 / (D_{p0}+D_{p1})T$
S_2/S_4	$T / (1+D_{p0}+D_{p1})T$
S_5/S_6	$D_{p0}T / (D_{p0}+1)T$
Q_1/Q_2	$D_{ss}T / (D_{ss}+1)T$
Q_4/Q_3	$(D_{s0}+D_{ss})T / (D_{s0}+D_{ss}+1)T$

D_{s0}. D_{p0} and D_{p1} are the duty ratio of 0 level and $\pm v_1$ level for H_1, respectively. Accordingly, the duty ratio of $\pm v_2/2$ level is $1-D_{p0}-D_{p1}$. Moreover, D_{s0} is the duty ratio of 0 level for H_2, and D_{ss} represents the phase shift ratio between H_1 and H_2. The sequence of the rising and falling edges of $v_p(t)$ and $v_s(t)$ determines the operating mode. According to the relationship of each control variable, NH3L-DAB can work in 12 different operating modes. The key waveforms of each mode for NH3L-DAB with $D_{ss} \in [0, 1]$ are shown in Figs. 3 and 4. Mode 4 is taken as an example to analyze the working principle of NH3L-DAB, and the specific waveforms are shown in Fig. 2. In Fig. 2, T is the half switching period, and the switching moments for each semiconductor devices are listed in Table I.

For NH3L-DAB, D_{p0}, D_{p1}, D_{s0}, and D_{ss} can be controlled independently to adjust the transmitted power P_t from v_1 to v_2. All the control variables, D_{p0}, D_{p1}, D_{s0}, and D_{ss}, are limited within the range [0, 1]; meanwhile, $D_{p0}+D_{p1} \leq 1$ as the duty ratio of $\pm v_1/2$ voltage level is $1-D_{p0}-D_{p1}$ and cannot be negative. In this article, the control coordinate $\boldsymbol{D}$ is used to denote the control variables (D_{p1}, D_{p0}, D_{s0}, D_{ss}), i.e., $\boldsymbol{D} = (D_{p1}, D_{p0}, D_{s0}, D_{ss})$. As illustrated in Fig. 2, there are ten subintervals within one switching period. Since the converter operation is odd symmetric for half switching cycle, i.e., $i_L(t) = -i_L(t+T)$, $v_p(t) = -v_p(t+T)$, and $v_s(t) = -v_s(t+T)$, only the subintervals for the first half-cycle from t_0 to t_5 are analyzed as follows.

Interval 1 [t_0, t_1]: The rising edge of S_1 is chosen as the beginning of switching period, i.e., t_0. During this interval, the switching devices S_1, S_2, S_5 are ON of H_1 side; meanwhile, Q_2 and Q_3 of H_2 side are ON. Accordingly, $v_p(t)$ is equal to 0, and $v_s(t)$ is $-v_2$. Then, $i_L(t) = i_L(t_0) + \frac{Nv_2}{L_s}t$.

Interval 2 [t_1, t_2]: At t_1, S_5 is turned OFF and S_6 is turned ON. During the commutation interval, $i_L(t)$ should be less than 0 to discharge the junction capacitor of S_6. Within interval 2, the switching devices S_1, S_2, S_6, Q_2, and Q_3 are ON. Hence, $v_p(t) = v_1$ and $v_s(t) = -v_2$. The inductor current $i_L(t)$ increase with the steepest slope in one switching period, i.e., $i_L(t) = i_L(t_1) + \frac{v_1+Nv_2}{L_s}t$.

Interval 3 [t_2, t_3]: Q_1 is turned ON and Q_2 is turned OFF at t_2. Hence, $v_s(t)$ is changed from $-v_2$ to 0. During this interval, the switching devices of H_1 have no action, and the slope of $i_L(t)$ is $\frac{v_1}{L_s}$.

TABLE II
CURRENT CONDITION OF THE INDUCTOR FOR THE SWITCHING DEVICES TO ACHIEVE ZVS

Switching Devices	Soft Switching Conditions
S_1, S_2, and S_6	$i_L(t)<0$
S_3, S_4, and S_5	$i_L(t)>0$
Q_1, Q_4	$i_L(t)>0$
Q_2, Q_3	$i_L(t)<0$

Interval 4 [t_3, t_4]: After Interval 3, $v_p(t)$ is equal to v_1, $v_s(t)$ becomes v_2 as Q_3 is turned OFF and Q_4 is turned ON at t_3. And the slew rate of $i_L(t)$ is reduced further, i.e., $\frac{v_1-Nv_2}{L_s}$.

Interval 5 [t_4, t_5]: S_1 is turned OFF and S_3 is turned ON at t_4. During the dead time, S_1 is OFF, the junction capacitor of S_3 can be discharged if $i_L(t) > 0$. Note that zero voltage switching (ZVS) of S_3 is not complete as $i_L(t)$ may discharge the junction capacitor of S_3 and S_4 from $v_1/2$ to $v_1/4$ simultaneously when S_1 is turned OFF and $i_L(t)$ is too small. Within interval 5, the switching devices S_2, S_3, S_6, Q_1, and Q_4 are ON. Hence, $v_p(t)$, $v_s(t)$ is equal to $v_1/2$ and v_2, respectively, and $i_L(t)$ can be calculated as $i_L(t) = i_L(t_4) + \frac{v_1-2Nv_2}{2L_s}t$.

Based on the above analysis, the corresponding prerequisite condition of each interval to realize ZVS for all switches can be deduced. The above analysis is applicable to the other working modes; no more explanation will be presented.

Based on the above analysis, the increment of $i_L(t)$ from t_0 to t_5 is

$$\Delta i_L=\left(\frac{v_1\left(1-D_{\mathrm{p0}}+D_{\mathrm{p1}}\right)}{2}-v_2\left(1-2D_{\mathrm{ss}}-D_{\mathrm{s0}}\right)\right)\times\frac{T}{L_{\mathrm{s}}}. \tag{1}$$

For NH3L-DAB converter, $i_L(t) = -i_L(t+\mathrm{T})$, we have $-i_L(t_0) = i_L(t_5) = \Delta i_L/2$. Then, the power transmitted from v_1 to v_2 and the rms value of inductor current can be expressed as

$$\begin{cases} P_{\mathrm{t}}(D) = \frac{1}{T}\int_0^T v_{\mathrm{p}}(t)\, i_{\mathrm{L}}(t)\, dt = \frac{1}{T}\int_0^T N v_{\mathrm{s}}(t)\, i_{\mathrm{L}}(t)\, dt \\ I_{\mathrm{rms}}(D) = \sqrt{\frac{1}{T}\int_0^T i_{\mathrm{L}}^2(t)\, dt}. \end{cases} \tag{2}$$

In order to get a more concise expression, P_{t} is normalized to be $P_{\mathrm{n,t}}$ as follows:

$$P_{\mathrm{t}} = \frac{N v_1 v_2 T}{4L_{\mathrm{s}}} \times P_{\mathrm{n,t}}. \tag{3}$$

For Modes 7–12 in Fig. 4, $1 \leq D_{\mathrm{ss}}+D_{\mathrm{s0}}$ is held. In these six modes, when $v_{\mathrm{p}}(t) \geq 0$, the case of $v_{\mathrm{s}}(t) \leq 0$ is always met, and vice versa. Therefore, the time interval for $v_{\mathrm{p}}(t) \times v_{\mathrm{s}}(t) > 0$ does not exist. It indicates that the power cannot be transmitted from H_1 to H_2 directly, leading to the relatively larger reactive power and conduction loss in Modes 7–12. Therefore, Modes 7–12 are not considered for optimizing the modulation method of NH3L-DAB converter.

From Fig. 3, compared with Mode 7 to Mode 12, $v_{\mathrm{p}}(t)$ and $v_{\mathrm{s}}(t)$ are overlapped with each other in Mode 1 to Mode 6, and then the power of them can be transferred more effectively. In these six modes, as shown in Fig. 3, the main difference is the control sequence of each switch. The prerequisite conditions for the direction of the inductor current $i_L(t)$ required for soft switching are presented in Table II, which is applicable to all modes. From Fig. 3, it is possible to achieve ZVS for all devices in Modes 1 and 4. But in the other modes, ZVS for all switches cannot be achieved. Therefore, these two modes will be selected to optimize the global rms value of the inductor current in Section IV for the forward power flow operation. Furthermore, the method in [45] will be used to verify that the switching devices can achieve ZVS completely.

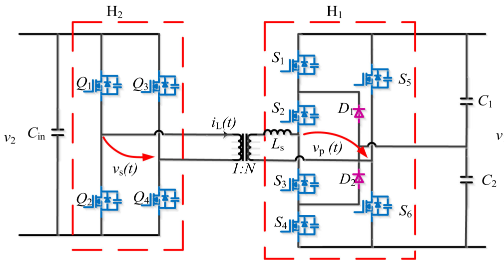

Fig. 5. Circuit topology of hybrid NPC three-level DAB converter in power reverse flow mode.

TABLE III
SWITCHING MOMENT FOR EACH SWITCHING DEVICE IN REVERSE MODE

Switching Device	Switching Moment
S_1/S_3	$(D_{\mathrm{p0}}+D_{\mathrm{p}})T\,/\,(1+D_{\mathrm{p0}})T$
S_2/S_4	$D_{\mathrm{p0}}T\,/\,(1+D_{\mathrm{p0}}+D_{\mathrm{p}})T$
S_5/S_6	$0\,/\,T$
Q_1/Q_2	$D_{\mathrm{ss}}T\,/\,(D_{\mathrm{ss}}+1)T$
Q_4/Q_3	$(D_{\mathrm{s0}}+D_{\mathrm{ss}})T\,/\,(D_{\mathrm{s0}}+D_{\mathrm{ss}}+1)T$

In addition to the 12 working modes described in Figs. 3 and 4, NH3L-DAB can also work in the two-level mode, i.e., S_1 and S_2 are turned ON or OFF at the same time, and so are S_3 and S_4. Detailed research work of 2L-DAB has been introduced in [19].

B. Basic Operating Principle for the NH3L-DAB Converter in Reverse Mode

For the convenience of analysis, the circuit topology and waveforms of reverse operation are redrawn in Fig. 5, and there are four control degrees too, which are redefined as D_{p}, D_{p0}, D_{s0}, D_{ss} in reverse operating mode. Among them, D_{p0} and D_{p} are the duty ratio of 0 level and $\pm v_1/2$ level for H_1, respectively. Accordingly, the duty ratio of $\pm v_1$ level is $1-D_{\mathrm{p0}}-D_{\mathrm{p}}$. Moreover, D_{s0} is the duty ratio of 0 level for H_2, and D_{ss} represents the phase shift between H_1 and H_2. The switching moments for each semiconductor devices are listed in Table III. $\boldsymbol{D}$ is used to represent the control coordinates $\boldsymbol{D} = (D_{\mathrm{p}}, D_{\mathrm{p0}}, D_{\mathrm{s0}}, D_{\mathrm{ss}})$. Based on the relationship of control valuables, it can be divided into 12 different operating modes for the converter. According to the analysis when the power flow is forward, Mode 1 is selected as the example to analyze the working principle of the converter. The typical waveform diagram of Mode 1 is shown in Fig. 6. The first half of the cycle can be divided into five stages from t_0 to t_5. The operating principle of each working stage will be discussed.

Interval 1 [t_0, t_1]: The rising edge of the driving signal of S_6 is chosen as the beginning of switching period t_0. During this

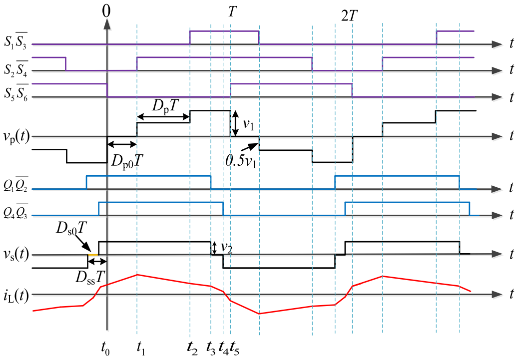

Fig. 6. Operating waveforms of NH3L-DAB converter in reverse mode.

interval, Q_1 Q_4, S_3, and S_4 are ON; meanwhile, S_6 is turned ON at t_0. Accordingly, $v_s(t)$ is equal to v_2, $v_p(t)$ is 0, and $i_L(t) = i_L(t_0) + \frac{Nv_2}{L_s}t$.

Interval 2 [t_1, t_2]: At t_1, S_4 is turned OFF and S_2 is ON. In order to achieve ZVS condition, $i_L(t)$ needs to be greater than 0 to discharge the junction capacitance of S_2. In stage 2, Q_1, Q_4, S_2, S_3, and S_6 are ON, so $v_s(t) = v_2$, $v_p(t) = v_1/2$, and $i_L(t) = i_L(t_1) + \frac{2Nv_2 - v_1}{2L_s}t$.

Interval 3 [t_2, t_3]: At t_2, S_3 is turned OFF and S_1 is turned ON, so v_p changes from $v_1/2$ to v_1, $v_s(t) = v_2$. The change rate of the inductor current $i_L(t)$ becomes larger, i.e., $\frac{Nv_2 - v_1}{L_s}$.

Interval 4 [t_3, t_4]: At t_3, Q_1 is turned OFF and Q_2 is turned ON. During this interval, the H_1 bridge has no action, $v_s(t) = 0$, $v_p(t) = v_1$.

Interval 5 [t_4, t_5]: At t_4, Q_3 is turned ON. $v_s(t) = -v_2$, $v_p(t) = v_1$. The inductor current $i_L(t)$ decrease with the steepest slope in one switching period, i.e., $\frac{-Nv_2 - v_1}{L_s}$.

Due to the symmetry of the positive and negative half-cycles, the detailed operation of the negative half-period will not be presented.

Based on the above analysis, from t_0 to t_5, the increment of i_L is expressed as

$$\Delta i_L = \left(\frac{(2D_{s0} + 4D_{ss} + 2)\,v_2 + (D_p + 2D_{p0} - 2)\,v_1}{4}\right) \times \frac{T}{L_s}. \tag{4}$$

The transferred power and the rms value of the inductor current of the reverse operation for the converter are shown as (2) and (3).

Among the 12 modes when the power reverse flows, the commonly and uncommonly used modes are shown in Figs. 7 and 8, respectively. When $D_{ss} \in [-1, 0]$, for Modes 9–12, as shown in Fig. 8, $v_p(t)$ and $v_s(t)$ do not have any overlapping area, so the power cannot be directly transferred, and both the backflow power and loss are greatly increased. Therefore, these modes will not be considered for optimizing the rms current.

To achieve better performance, Modes 1–8 are selected in reverse power flow mode. The key waveforms in these modes are shown in Fig. 7. When the power is transmitted in the reverse direction, it is possible for all the devices to realize soft switching in Mode 1, Mode 2, and Mode 3. Therefore, these modes will be used to optimize the global rms value of the current in Section V.

III. PERFORMANCE BARRIERS OF CONVENTIONAL 2L-DAB CONVERTER

Fig. 9 illustrates the schematic of isolated dc/dc converter with ideal transformer, which consists of a primary inverter, a secondary rectifier, and an ideal transformer. To simplify the analysis, the turns ratio of the high-frequency transformer is assumed to be 1. Afterward, two indices are introduced to describe the performance of isolated dc–dc converter: the relative rms current factor λ_{rms} and the relative current stress factor λ_{cst}. The definitions are as follows:

$$\begin{cases} \lambda_{\text{rms}} = \frac{1}{T_{\text{iso}}} \int_0^{T_{\text{iso}}} \left(\frac{i_{\text{T,ac}}(t)}{I_{\text{T,o,avg}}}\right)^2 dt \\ \lambda_{\text{cst}} = \frac{i_{\text{T,ac,peak}}}{I_{\text{T,o,avg}}} \end{cases} \tag{5}$$

where T_{iso} is the converter switching period, $i_{\text{T,ac}}(t)$ represents the ac current through the ideal transformer (as shown in Fig. 9), and $i_{\text{T,ac,peak}}$ is referred to the peak value of $i_{\text{T,ac}}(t)$ within one switching period. $I_{\text{T,o,avg}}$ denotes the averaging value of output current. It can be seen that λ_{rms} is proportional to the conduction loss. Moreover, for DAB converter, λ_{cst} relates to the switching loss.

If $i_{\text{T,ac}}(t)$ is a pure ac square wave with 50% duty ratio and the secondary rectifier can work as an ideal rectifier, both λ_{rms} and λ_{cst} can achieve the minimum value, i.e., However, in practical implementations, $i_{\text{T,ac}}(t)$ is usually the sinusoidal waveforms, trapezoid waveforms, or triangle waveforms. In such conditions, λ_{rms} and λ_{cst} will be larger than 1, leading to the additional conduction losses and current stress.

In this article, we focus on an automotive application [41]: the high-voltage (HV) dc bus varies from 200 to 460 V, and the low-voltage (LV) dc bus ranges from 20 to 28.8 V. As shown in Fig. 10, the maximum and the minimum voltage transmission ratio are $M_{\max} = \frac{28.8N}{200}$ and $M_{\min} = \frac{20N}{460}$, respectively, where N is the turns ratio of high-frequency transformer. The voltage transmission ratio for this application has large variation, and we have

$$\gamma = \frac{28.8 \times N}{200} \times \frac{460}{20 \times N} = 3.31. \tag{6}$$

For designing 2L-DAB converter, M is the critical parameter. By choosing the turns ratio of high-frequency transformer, $M_{\max}$ and $M_{\min}$ can be set. It is preferred that both $M_{\max}$ and $M_{\min}$ are close to 1 as the 2L-DAB converter can achieve wide soft-switching range and small rms current when M is near 1. However, since γ is equal to $M_{\max}/M_{\min}$, $M_{\max}$ is larger than $\sqrt{\gamma}$ when N is designed to make $M_{\min} \in [1/\sqrt{\gamma}, 1]$, or $M_{\min}$ is smaller than $1/\sqrt{\gamma}$ when $M_{\max} \in [1, \sqrt{\gamma}]$. In another word, no matter how much N is equal to, $M_{\max}$ has to be larger than $\sqrt{\gamma}$ or $M_{\min}$ should be less than $1/\sqrt{\gamma}$. For instance, at $M_{\min}$ $=1/\sqrt{\gamma} = 0.55$, λ_{rms} and λ_{cst} of 2L-DAB converter, with the optimal modulation schemes in [14] and [19] to minimize the rms current, are illustrated in Fig. 11. As the figures show, both λ_{rms} and λ_{cst} are much larger than 1, indicating that the 2L-DAB converter has large conduction losses and switching losses. The curves in Fig. 11 can be regarded as the performance barriers of 2L-DAB converter. From further theoretically analysis, it can be found that the performance of 2L-DAB converter has significant

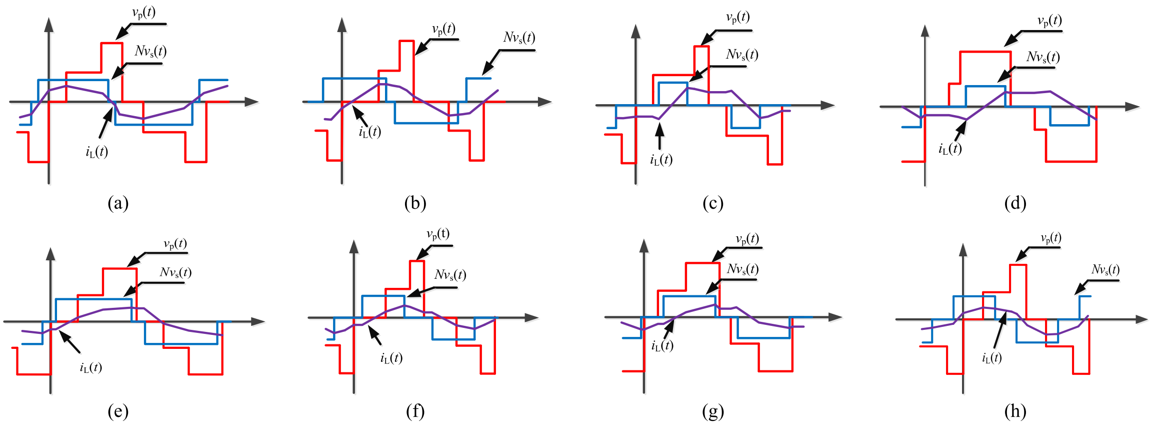

Fig. 7. Operating waveforms of eight common operating modes in reverse power flow. (a) Mode 1. (b) Mode 2. (c) Mode 3. (d) Mode 4. (e) Mode 5. (f) Mode 6. (g) Mode 7. (h) Mode 8.

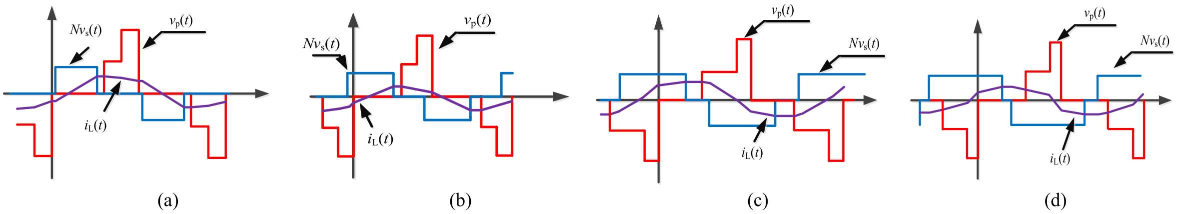

Fig. 8. Operating waveforms of four uncommon operating modes in reverse power flow. (a) Mode 9. (b) Mode 10. (c) Mode 11. (d) Mode 12.

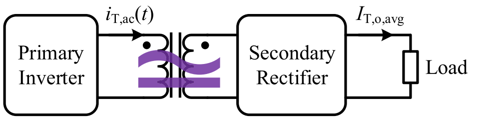

Fig. 9. Schematic of isolated dc/dc converter with ideal transformer.

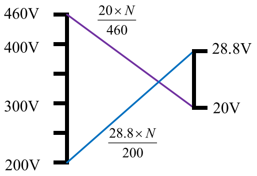

Fig. 10. Voltage transmission ratio for variable input/output voltage.

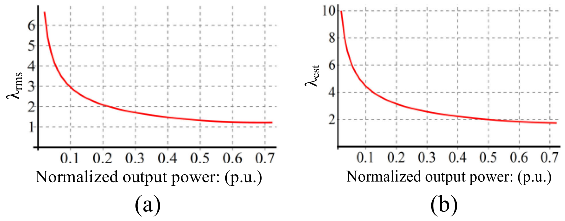

Fig. 11. Design limitation of 2L-DAB converter. (a) λ_{rms}. (b) λ_{cst}.

decrement when M is far away from 1. Hence, the 2L-DAB is less suitable for such wide voltage range applications.

By taking advantages of multilevel topology, NH3L-DAB can break the design limitation of 2L-DAB converter. Fig. 12 illustrates the comparisons between inductor current of 2L-DAB and that of NH3L-DAB with $M = 0.56$ and the same output power. As the figure shows, NH3L-DAB converter can achieve 37.4% λ_{rms} reduction and 46.9% λ_{cst} reduction. Hence, the three-level topology is a promising alternative for such wide voltage range applications.

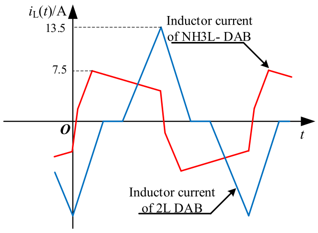

Fig. 12. Comparison between $i_L(t)$ of 2L-DAB and that of NH3L-DAB with the same M and output power and the same circuit parameters ($v_1 = 400$ V and $P_{\text{n,t}} = 0.3$).

IV. OPTIMAL MODULATION SCHEME FOR MINIMIZING THE RMS VALUE OF INDUCTOR CURRENT IN FORWARD OPERATION

In order to achieve higher efficiency, the four control variables of NH3L-DAB converter, ($D_{\text{p0}}, D_{\text{p1}}, D_{\text{s0}}, D_{\text{ss}}$), should be carefully coordinated. In this article, we focus on deriving the modulation strategies to minimize the conduction losses, i.e., the rms value of inductor current. Afterward, the condition for ZVS of all semiconductor switches in each mode will be discussed.

A. GOC Equation and the Modulation Optimization

The control coordinates that can minimize the conduction losses for given P_{set} and M can be derived by solving the following optimization problem:

$$\begin{aligned}&\text{minimize}\, I_{2\mathrm{rms}}\left(D_{\mathrm{p1}}, D_{\mathrm{p0}}, D_{\mathrm{ss}}, D_{\mathrm{s0}}\right)\\&\text{subject to}\, P_{\mathrm{n,t}}\left(D_{\mathrm{p1}}, D_{\mathrm{p0}}, D_{\mathrm{ss}}, D_{\mathrm{s0}}\right) = P_{\mathrm{set}}\end{aligned} \tag{7}$$

where $I_{2\mathrm{rms}}(\mathbf{D}) = (I_{\mathrm{rms}}(\mathbf{D}))^2$. Since $I_{2\mathrm{rms}}$ is proportional to the conduction losses, it is convenient to use $I_{2\mathrm{rms}}$ as the objective function. As pointed out in [19], for the solution of (7), the following GOC equations should be satisfied:

$$\xi_{D\mathrm{p1}} = \xi_{D\mathrm{p0}} = \xi_{D\mathrm{ss}} = \xi_{D\mathrm{s0}} \tag{8}$$

where $\xi_{D\mathrm{x}}(D_{\mathrm{p1}}, D_{\mathrm{p0}}, D_{\mathrm{ss}}, D_{\mathrm{s0}}) = \frac{\frac{\partial I_{2\mathrm{rms}}(D_{\mathrm{p1}}, D_{\mathrm{p0}}, D_{\mathrm{ss}}, D_{\mathrm{s0}})}{\partial D_{\mathrm{x}}}}{\frac{\partial P_{\mathrm{n,t}}(D_{\mathrm{p1}}, D_{\mathrm{p0}}, D_{\mathrm{ss}}, D_{\mathrm{s0}})}{\partial D_{\mathrm{x}}}}$, D_{x} is referred to one control variable, $D_{\mathrm{x}} \in \{D_{\mathrm{p1}}, D_{\mathrm{p0}}, D_{\mathrm{s0}}, D_{\mathrm{ss}}\}$. ξ depicts the ratio of the cost (i.e., the increment of $I_{2\mathrm{rms}}$) to the gain (i.e., the increment of $P_{\mathrm{n,t}}$) induced by a small perturbation of control variables. With respect to $\boldsymbol{D}_{\mathrm{opt}}$, the cost-gain ratio of all these four control variables should be equal to each other based on (8).

For example, at a given control coordinate $\boldsymbol{D}^* = (D^*{}_{\mathrm{p0}}, D^*{}_{\mathrm{p1}}, D^*{}_{\mathrm{s0}}, D^*{}_{\mathrm{ss}})$, if $\xi_{D\mathrm{p1}}(\mathbf{D}^*) < \xi_{D\mathrm{ss}}(\mathbf{D}^*)$, it means

$$\left(\frac{\partial I_{2\mathrm{rms}}}{\partial D_{\mathrm{ss}}} : \frac{\partial P_{\mathrm{n,t}}}{\partial D_{\mathrm{ss}}}\right) > \left(\frac{\partial I_{2\mathrm{rms}}}{\partial D_{\mathrm{p1}}} : \frac{\partial P_{\mathrm{n,t}}}{\partial D_{\mathrm{p1}}}\right) > 0. \tag{9}$$

Considering another control coordinate $\mathbf{D}'$ at the neighborhood of $\boldsymbol{D}^*$, and $\mathbf{D}'$ is given as follows:

$$\mathbf{D}' = \left(D^*_{\mathrm{p1}} + \frac{\partial P_{\mathrm{n,t}}}{\partial D_{\mathrm{ss}}} \times \Delta d, D^*_{\mathrm{p0}}, D^*_{\mathrm{ss}} - \frac{\partial P_{\mathrm{n,t}}}{\partial D_{\mathrm{p1}}} \times \Delta d, D^*_{\mathrm{s0}}\right) \tag{10}$$

where Δd represents the small variation of control variables. The power and the rms current of $\mathbf{D}'$ can be expressed as follows:

$$\begin{aligned}&P_{\mathrm{n,t}}(\mathbf{D}') \approx P_{\mathrm{n,t}}(\mathbf{D}^*)\\&-\frac{\partial P_{\mathrm{n,t}}}{\partial D_{\mathrm{p1}}} \times \frac{\partial P_{\mathrm{n,t}}}{\partial D_{\mathrm{ss}}}\Delta d + \frac{\partial P_{\mathrm{n,t}}}{\partial D_{\mathrm{ss}}} \times \frac{\partial P_{\mathrm{n,t}}}{\partial D_{\mathrm{p1}}}\Delta d = P_{\mathrm{n,t}}(\mathbf{D}^*)\end{aligned} \tag{11}$$

$$\begin{aligned}&I_{2\mathrm{n,rms}}(\mathbf{D}') \approx I_{2\mathrm{n,rms}}(\mathbf{D}^*)\\&-\frac{\partial I_{2\mathrm{rms}}}{\partial D_{\mathrm{ss}}} \times \frac{\partial P_{\mathrm{n,t}}}{\partial D_{\mathrm{p1}}}\Delta d + \frac{\partial I_{2\mathrm{rms}}}{\partial D_{\mathrm{p1}}} \times \frac{\partial P_{\mathrm{n,t}}}{\partial D_{\mathrm{ss}}}\Delta d.\end{aligned} \tag{12}$$

By applying (18) to (21), it can be found that

$$I_{2\mathrm{rms}}(\mathbf{D}^*) > I_{2\mathrm{rms}}(\mathbf{D}'). \tag{13}$$

Equations (12) and (13) indicate that $\mathbf{D}'$ has less rms current than $\boldsymbol{D}^*$; meanwhile, the transmitted power of these two control coordinates is the same. Hence, $\mathbf{D}'$ is "better" than $\boldsymbol{D}^*$. Based on above analysis, the optimal control coordinate $\boldsymbol{D}_{\mathrm{opt}} = (D_{\mathrm{p1,opt}}, D_{\mathrm{p0,opt}}, D_{\mathrm{s0,opt}}, D_{\mathrm{ss,opt}})$ with respect to the minimized rms current should meet the constraint in (7).

In the derivation of the optimal modulation schemes, M is the critical parameter as it can determine whether a solution is effective. Therefore, the cases of $0 \le M \le 0.5$, $0.5 \le M \le 1$, and $M > 1$ should be discussed separately, which are divided according to the relationship of input and output voltage. For example, the case of $0 \le M \le 0.5$ implies that the output voltage is less than the medium voltage level of the primary bridge, i.e., $N \times v_2 < v_1/2$, and $0.5 \le M \le 1$ indicates that $N \times v_2$ is larger than $v_1/2$ level. Moreover, by calculating and analyzing $\xi_{D\mathrm{x}}$ for each operating mode, it can be concluded that all the optimal control coordinates $\boldsymbol{D}_{\mathrm{opt}}$ are located in Modes 1 and 4 when $M < 1$. Additionally, it should be pointed out that Modes 1 and 4 can achieve soft switching and cover the whole power range, i.e., $P_{\mathrm{n,t}} \in [0, 1]$. The definition domain and power transmission functions of Modes 1 and 4 are presented in Table IV, and the relevant analysis of other modes is presented in Table IX in the Appendix.

TABLE IV
DEFINITION DOMAIN AND POWER TRANSMISSION FUNCTIONS OF MODES 1 AND 4

Mode	Definition Domain	Power Transmission Function
1	$0 \le D_{ss} \le D_{ss} + D_{s0} \le$ $D_{p0} \le D_{p0} + D_{p1} \le 1$	$P_{M1} = \frac{TNv_1v_2}{4L_s} \times \begin{pmatrix} D_{p0}^2 - D_{p1}^2 + D_{s0} + 2D_{ss} \\ +D_{p1}\left(1 + D_{s0} + 2D_{ss}\right) \\ -D_{p0}\left(1 + 2D_{p1} + D_{s0} + 2D_{ss}\right) \end{pmatrix}$
4	$0 \le D_{p0} \le D_{ss} \le D_{ss}$ $+D_{s0} \le D_{p0} + D_{p1} \le 1$	$P_{M4} = \frac{TNv_1v_2}{4L_s} \times \begin{pmatrix} -3D_{p0}^2 - D_{p1}^2 + D_{s0} - 2D_{s0}^2 + 2D_{ss} \\ -D_{p0}\left(1 + 2D_{p1} - 3D_{s0} - 6D_{ss}\right) - 4D_{ss}^2 \\ -4D_{s0}D_{ss} + D_{p1}\left(1 + D_{s0} + 2D_{ss}\right) \end{pmatrix}$

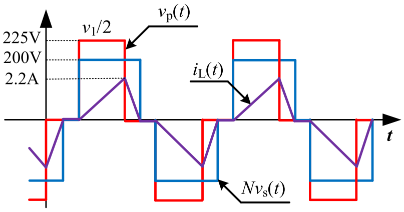

Fig. 13. Typical waveforms of NH3L-DAB converter with the modulation scheme in (18) ($P_{\mathrm{n,t}} = 0.032$ and $Nv_2 = 200$ V).

B. Modulation Optimization for $0 \le \mathrm{M} \le 0.5$

By solving the GOC equation at Mode 1, it can be found that, with $0 \le M \le 0.5$, the optimal control coordinates with respect to the minimum rms current should meet the following constraints:

$$\begin{aligned}D_{\mathrm{p1,opt}} &= 0\\D_{\mathrm{ss,opt}} &= \left(1 - D_{\mathrm{s0,opt}}\right)\left(1 - 2M\right)\\D_{\mathrm{p0,opt}} &= \left(1 - D_{\mathrm{s0,opt}}\right)\left(1 - 2M\right) + D_{\mathrm{s0,opt}}.\end{aligned} \tag{14}$$

Note that the effective solution of (7) should range from 0 to 1. According to (14), since D_{s0} should range from 0 to 1, D_{ss} and D_{p0} are located within $[0, 1-2M]$ and $[1-2M, 1]$, respectively. And the normalized power $P_{\mathrm{n,t}}$ is limited within $[0, 2M(1-2M)]$. Then, the power range for (14) is regarded as the light load range.

Fig. 13 illustrates the operating waveforms for the optimal control coordinates in (14). Since $D_{\mathrm{p1}} = 0$, the duty ratio for the voltage level $\pm v_1$ is zero. NH3L-DAB converter operates similar to the 2L-DAB converter with $v_1/2$ input voltage. In the light load range, $v_{\mathrm{p}}(t)$ and $v_{\mathrm{s}}(t)$ are of voltage matching state [13], which means the averaging value of $v_{\mathrm{p}}(t)$ in $[0, T]$ is equal to the averaging value of $v_{\mathrm{s}}(t)$ in $[D_{\mathrm{ss}}T, (1+D_{\mathrm{ss}})T]$, i.e.,

$$v_{\mathrm{in}} \times \frac{1 + D_{\mathrm{p1}} - D_{\mathrm{p0}}}{2} = Nv_{\mathrm{o}} \times \left(1 - D_{\mathrm{s0}}\right). \tag{15}$$

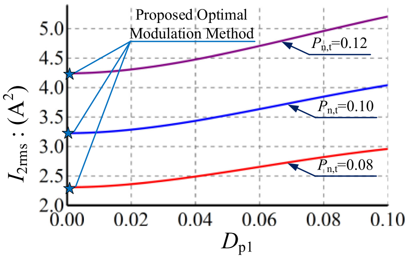

Fig. 14. Curves of $I_{2\mathrm{rms}}$ versus D_{p1} with meeting the voltage matching condition in (15).

However, (14) is not the unique solution for voltage matching state when $N \times v_2 < v_1/2$. The voltage matching state condition (10) can also be met by adding D_{p1} and correspondingly adjusting D_{p0}. As $M = 0.3$, Fig. 14 plots the curves of $I_{2\mathrm{rms}}$ versus D_{p1} when the voltage matching condition in (15) is satisfied, and $P_{\mathrm{n,t}}$ remains constant for each curve. As Fig. 14 shows, the increment of D_{p1} leads to an increment of $I_{2\mathrm{rms}}$. Hence, the minimum $I_{2\mathrm{rms}}$ at voltage matching state is obtained at $D_{\mathrm{p1}} = 0$, i.e., the solutions of GOC equation in (8).

When the optimal modulation scheme (14) is used, the current at each switching moment is given as follows:

$$\begin{cases} i_L(0) = -(1 - D_{\mathrm{s0}})(1 - 2M)M \times \frac{v_{\mathrm{in}}T}{L_{\mathrm{s}}} \\ i_L(D_{\mathrm{ss}}T) = i_L(D_{\mathrm{p0}}T) = 0 \\ i_L((D_{\mathrm{p1}} + D_{\mathrm{p0}})T) = i_L((D_{\mathrm{ss}} + D_{\mathrm{s0}})T) = 0 \\ i_L(T) = (1 - D_{\mathrm{s0}})(1 - 2M)M \times \frac{v_{\mathrm{in}}T}{L_{\mathrm{s}}}. \end{cases} \tag{16}$$

It can be seen that Q$_1$–Q$_4$ can achieve zero current switching (ZCS) in the converter. In the HV side, the condition of complete ZVS of the devices in the three-level bridge arm and two-level bridge arm can be verified according to [45] and Table II when considering the junction capacitor of switches. However, the value of the junction capacitance will change with the change of V_{DS}. Table II presents the prerequisite conditions for the all switches to achieve ZVS. In the experimental implementation, the current is selected based on the method introduced in [45].

As pointed out in [1], [42], and [43], for the applications that the Q$_1$–Q$_4$ are of LV and high current, the turned-OFF losses resulted from the stray inductance are the major part of the MOSFETs switching losses. Therefore, the switching losses of the LV side can be significantly reduced by ZCS for such applications.

For the modulation schemes in (14), both D_{s0} and D_{p0} decrease monotonically while increasing $P_{\mathrm{n,t}}$. When the transmitted power is larger than the upper boundary of light load range, D_{p0} will decrease further; meanwhile, D_{s0} is kept at 0, resulting that $D_{\mathrm{ss}} > D_{\mathrm{p0}}$. Then, NH3L-DAB converter goes to Mode 4. The operating mode following the light load range is named as medium load range.

At medium load range, the curved surface of $I_{2\mathrm{rms}}$ versus D_{p1} and D_{p0} is illustrated in Fig. 15. In this scenario, $P_{\mathrm{n,t}} = 0.5$, $M = 0.3$, and $D_{\mathrm{s0}} = 0$; meanwhile, D_{ss} is calculated according to $P_{\mathrm{n,t}}, D_{\mathrm{p1}}$, and D_{p0}. As can be observed, $I_{2\mathrm{rms}}$ has a unique global minimum point. By solving the GOC equation (8) in Mode 4, the control coordinate for minimum $I_{2\mathrm{rms}}$ can be derived as

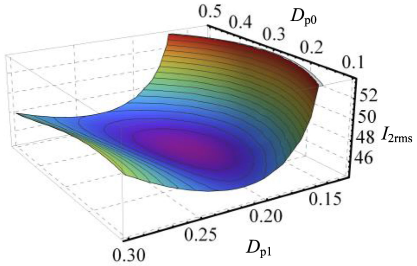

Fig. 15. Curved surface of $I_{2\mathrm{rms}}$ versus D_{p1} and D_{p0} when $P_{\mathrm{n,t}} = 0.5$ and $M = 0.3$.

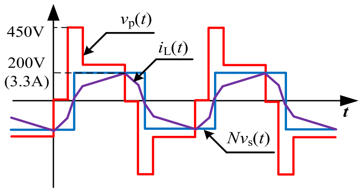

Fig. 16. Typical waveforms of NH3L-DAB converter with the modulation scheme in (17) for Mode 4 ($P_{\mathrm{n,t}} = 0.14$ and $Nv_2 = 200$ V).

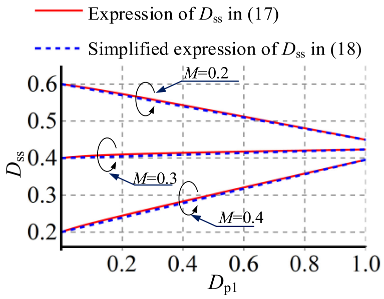

Fig. 17. Comparisons of D_{ss} calculated by (17) and (18).

$$\begin{aligned} D_{\mathrm{s0,opt}} &= 0 \\ D_{\mathrm{p0,opt}} &= (1 - 2M)(1 - D_{\mathrm{p1,opt}}) \\ D_{\mathrm{ss,opt}} &= \frac{D_{\mathrm{p1,opt}}\left(2M^2 - 1\right) + M(1 - 2M)}{2M} \\ &+ \frac{\sqrt{(1-2M)^2 M^2 + 2D_{\mathrm{p1,opt}} M(1 - 3M + 4M^2 - 4M^3)}}{2M} \\ &+ \frac{\sqrt{+D_{\mathrm{p1,opt}}^2 (1 - 2M + 4M^2 - 4M^3 + 4M^4)}}{2M}. \end{aligned} \tag{17}$$

And the corresponding operating waveforms are illustrated in Fig. 16. Moreover, to reduce the calculation complexity, the function of D_{ss} in (17) can be well approximated by a linear function as follows:

$$\begin{aligned} &D_{\mathrm{ss,app}} \\ &= (1 - 2M) + D_{\mathrm{p1,opt}} \times \frac{\sqrt{1 - M^2 + 4M^2} - 1 - M}{2M}. \end{aligned} \tag{18}$$

Fig. 17 shows the curve of D_{ss} versus D_{p1} with different M in Mode 4. It can be seen that the results calculated from (17) and (18) are almost identical.

By using the simplified expressions of $D_{\rm ss}$ in (18), the current at each switching instance can be given as follows, (19) shown at bottom of the next page.

According to the ZVS conditions of each switching devices, it can be verified that all the switching devices, S_1–S_6 and Q_1–Q_4, have the possibility to achieve complete ZVS. Moreover, for the switching moments for Q_1–Q_4, i.e., $D_{\rm ss}T$ and $(D_{\rm s0}+D_{\rm ss})T$, it can be found that the maximum value of $\frac{M\sqrt{1-M^2}}{1+\sqrt{1-M^2}}$ is only 0.23 when $M\in[0, 1]$, hence, the switching current of Q_1–Q_4 can be limited, it helps to reduce the turned-OFF losses of Q_1–Q_4 for the applications that are of LV and high current.

Moreover, $D_{\rm p1}$ should be within the range [0, 1]; accordingly, the ranges of $D_{\rm p0}$ and $D_{\rm ss}$ are $[0, 1-2M]$ and $[1-2M, \frac{\sqrt{1-M^2}-1+M}{2M}]$, respectively. Then, the power range for the medium load is expressed as

$$P_{\rm n,t} \in \left[2M\left(1-2M\right), \frac{2\left(\sqrt{1-M^2}-1+M^2\right)}{M^2}\right]. \qquad (20)$$

With respect to the optimal control coordinate at the boundary between the light load range and medium load range, the control coordinate is $\boldsymbol{D}_{\rm opt} = (0, 1-2M, 0, 1-2M)$, which can meet the expressions in both (14) and (17). Hence, the optimal control coordinates continuously vary from light load to medium load. The light-load and medium-load boundaries are denoted as BA1 and BA2.

If $P_{\rm n,t}$ is even higher than the upper boundary of the medium load range, NH3L-DAB will work at heavy load range. By solving the GOC equations, it can be found that the optimal control coordinates are given as

$$\begin{aligned} D_{\rm s0,opt} &= D_{\rm p0,opt} = 0 \\ D_{\rm p1,opt} &= 1. \end{aligned} \qquad (21)$$

In the heavy load range, only $D_{\rm ss}$ is used to adjust the output power, and other control variables keep invariant. Then, both $v_{\rm p}(t)$ and $v_{\rm s}(t)$ are the standard ac square waves with 0.5 duty ratio. For the modulation in (21), the switching current is given as follows, (27) shown at the bottom of the next page.

$$\begin{cases} i_L\left(0\right) = i_L\left(D_{\rm p0}T\right) = -\left(1+\left(2D_{\rm ss}-1\right)M\right) \times \frac{v_{\rm in}T}{2L_{\rm s}} \\ i_L\left(D_{\rm ss}T\right) = i_L\left(\left(D_{\rm ss}+D_{\rm s0}\right)T\right) \\ = \left(2D_{\rm ss}+M-1\right) \times \frac{v_{\rm in}T}{2L_{\rm s}} \\ i_L\left(\left(D_{\rm p0}+D_{\rm p1}\right)T\right) = \left(1+\left(2D_{\rm ss}-1\right)M\right) \times \frac{v_{\rm in}T}{2L_{\rm s}}. \end{cases} \qquad (22)$$

Since $D_{\rm ss}$ ranges between $\frac{\sqrt{1-M^2}-1+M^2}{2M}$ and $\frac{1}{2}$ in the heavy load range, we have $i_L(0) = i_L(D_{\rm p0}T) < 0$, $i_L((D_{\rm p0}+D_{\rm p1})T) > 0$, and $i_L(D_{\rm ss}T) = i_L((D_{\rm ss}+D_{\rm s0})T) > 0$. Then, ZVS of all switching devices can be achieved. The corresponding operating waveforms are illustrated in Fig. 18.

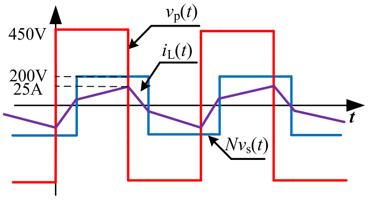

Fig. 18. Typical waveform of NH3L-DAB working in two-level single phase shift (SPS) mode ($P_{\rm n,t} = 0.95$ and $Nv_2 = 200$ V).

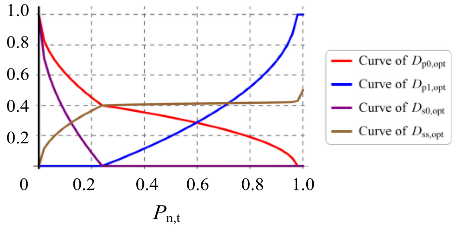

Fig. 19. Trajectories of optimal control variables versus transmitted power in the case $0 \leq M \leq 0.5$ ($M = 0.3$).

Such control scheme is the same as SPS modulation scheme of the 2L-DAB converter that has been investigated comprehensively in the literature. Then, we will not go further to discuss this scenario.

Combining (14), (17), and (21), the closed-form solutions of $\boldsymbol{D}_{\rm opt}$ in the case of $0 \leq M \leq 0.5$ are obtained. With given M, there is a unique solution $\boldsymbol{D}_{\rm opt}$ for each normalized transmitted power point. The trajectories of all four control variables versus $P_{\rm n,t}$ are illustrated in Fig. 19 with $M = 0.3$.

C. Modulation Optimization for 0.5 ≤ M ≤ 1

In the case of $0.5 \leq M \leq 1$, it indicates that $v_1/2 < N \times v_2 < v_1$. By solving the GOC equation at Mode 1, the optimal control coordinates to minimize the rms current can be expressed as follows:

$$\begin{aligned} D_{\rm ss} &= 0 \\ D_{\rm s0} &= D_{\rm p0} \\ D_{\rm p1} &= \left(2M-1\right)\left(1-D_{\rm p0}\right). \end{aligned} \qquad (23)$$

Both $D_{\rm s0}$ and $D_{\rm p0}$ are within [0, 1], and $D_{\rm p1}$ ranges between 0 and $2M-1$. Accordingly, the power range for light load is $[0, 2(1-M)(2M-1)]$. The expressions of $i_L(t)$ at switching moment are given as

$$\begin{cases} i_L\left(0\right) = i_L\left(D_{\rm ss}T\right) \\ = i_L\left(D_{\rm p0}T\right) = i_L\left(\left(D_{\rm ss}+D_{\rm s0}\right)T\right) = 0 \\ i_L\left(\left(D_{\rm p0}+D_{\rm p1}\right)T\right) \\ = \left(1-D_{\rm p0}\right)\left(1-M\right)\left(2M-1\right) \times \frac{v_1T}{L_{\rm s}}. \end{cases} \qquad (24)$$

It is similar to the light load range in the case of $0 \leq M \leq 0.5$. In this scenario, the prerequisite condition of ZVS for S_1 and S_3 can be verified by Table II; meanwhile, S_2, S_4–S_6,

$$\begin{cases} i_L\left(0\right) = \left(4\left(1-D_{\rm p1}\right)M^2 - 2\left(1-D_{\rm p1}\right)M - D_{\rm p1}\sqrt{1-M^2}\right) \times \frac{v_{\rm in}T}{2L_{\rm s}} \\ i_L\left(D_{\rm p0}T\right) = -D_{\rm p1}\sqrt{1-M^2} \times \frac{v_{\rm in}T}{2L_{\rm s}} \\ i_L\left(D_{\rm ss}T\right) = i_L\left(\left(D_{\rm ss}+D_{\rm s0}\right)T\right) = \frac{D_{\rm p1}M\sqrt{1-M^2}}{1+\sqrt{1-M^2}} \times \frac{v_{\rm in}T}{2L_{\rm s}} \\ i_L\left(\left(D_{\rm p0}+D_{\rm p1}\right)T\right) = D_{\rm p1}\sqrt{1-M^2} \times \frac{v_{\rm in}T}{2L_{\rm s}} \end{cases} \qquad (19)$$

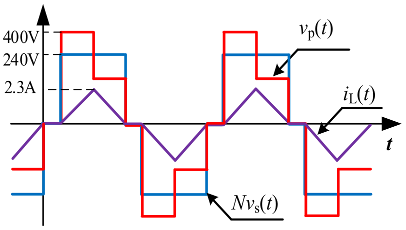

Fig. 20. Typical waveforms of NH3L-DAB converter with the modulation scheme in (27) ($P_{n,t} = 0.048$ and $Nv_2 = 240$ V).

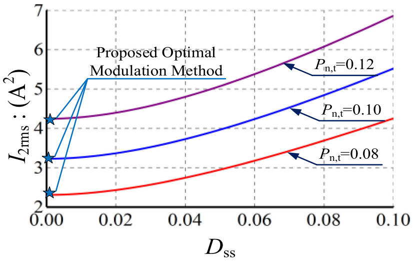

Fig. 21. Curves of I_{2rms} versus D_{ss} with meeting the voltage matching condition in (15) with $M = 0.7$.

and Q$_1$–Q$_4$ can achieve ZCS. Fig. 20 illustrates the operating waveforms for the optimal control coordinates in (23). It can be found that the modulation scheme in (23) also meets the voltage matching constraint as (15). Then, the NH3L-DAB converter also operates at voltage matching state. As the figures show, $i_L(t)$ is a triangle wave, and the backflow power is eliminated. Moreover, Fig. 21 demonstrates the curves of I_{2rms} versus D_{ss}; meanwhile, the other control variables are set to meet the voltage matching condition (15) at $M = 0.7$. However, as the figure shows, the increment of D_{ss} leads to increasing I_{2rms}. It implies that, to achieve minimum rms current, D_{ss} should be kept at zero.

When the power exceeds the light load range, D_{p1} and D_{ss} should become larger to make the output power track the reference; meanwhile, D_{s0} and D_{p0} are equal to 0. Hence, the NH3L-DAB converter operates in Mode 4. By solving the GOC equation, the expressions of the optimal control coordinate are given as follows:

$$\begin{aligned} &D_{s0,opt} = D_{p0,opt} = 0\\ &D_{ss,opt} = \tfrac{D_{p1,opt}(M-1)}{2M}\\ &+\tfrac{\sqrt{M\left(D_{p1,opt}+D^2_{p1,opt}-2D_{p1,opt}M\right)+D^2_{p1,opt}(1-M)^2}}{2M}. \end{aligned} \tag{25}$$

With respect to the ranges of each control variable, D_{p1} is within [$2M$−1, 1], and D_{ss} ranges from 0 to $\frac{\sqrt{1-M^2}-1+M}{2M}$. Accordingly, the power range for medium load is given as

$$P_{n,t} \in \left[2\left(1-M\right)\left(2M-1\right), \frac{2\left(\sqrt{1-M^2}-1+M^2\right)}{M^2}\right]. \tag{26}$$

The above-mentioned power boundary is denoted as BB1 and BB2.

Fig. 22 depicts the curves of I_{2rms} versus D_{p1} with $M = 0.7$; meanwhile, $P_{n,t}$ is constant for each curve. For voltage matching control, D_{p1} is kept at 0.4; meanwhile, both D_{s0} and D_{p0} are 0.

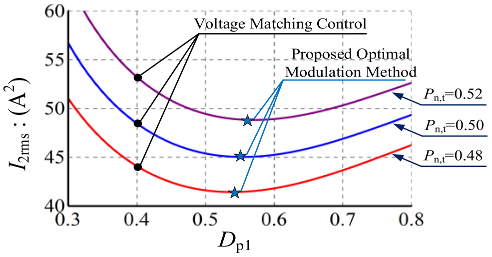

Fig. 22. Curves of I_{2rms} versus D_{p1} with $D_{p0} = D_{s0} = 0$ when $M = 0.7$.

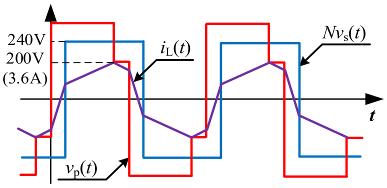

Fig. 23. Typical waveforms of NH3L-DAB converter with the modulation scheme in (29) ($P_{n,t} = 0.192$ and $Nv_2 = 240$ V).

As can be observed, rms current of the proposed $\boldsymbol{D}_{opt}$ is smaller than that of the voltage matching control.

The typical waveforms of NH3L-DAB converter with the modulation scheme in (25) are illustrated in Fig. 23. The switching current is given as follows:

Note that D_{ss} in (27) is calculated according to the second function in (25). It can be demonstrated that, with the proposed modulation scheme, the switching current meets the ZVS conditions for all switching devices.

If the normalized power exceeds the upper bound of the medium load range, the solution of GOC equation is equal to the SPS modulation scheme in (21), which has been discussed in the case of $0 \le M \le 0.5$.

Combining the expressions in (21), (23), and (25), the closed-form expressions of $\boldsymbol{D}_{opt}$ in the case of $0.5 < M \le 1$ are obtained. And the trajectories of all four control variables ($D_{p0,opt}$, $D_{p1,opt}$, $D_{s0,opt}$, $D_{ss,opt}$) versus $P_{n,t}$ are illustrated in Fig. 24 with $M = 0.7$. In this scenario, $D_{p0,opt}$ is equal to $D_{s0,opt}$ for all operating points.

D. Synthesis of the Optimal Modulation Method

In Fig. 25, curves of power ranges for the light load, medium load, and heavy load versus M are illustrated. These three load patterns cover the whole power range of NH3L-DAB without overlapping or vacancy. The heavy load range of NH3L-DAB is the same as that of the conventional 2L-DAB converter [19]. However, the light load range is much smaller, and the medium load range is enlarged significantly.

When M is equal to 0.5, the range of light load is 0; NH3L-DAB converter mainly operates at medium load range. Fig. 26 illustrates the comparisons of λ_{rms} and λ_{cst} of NH3L-DAB and that of the conventional 2L-DAB at $M = 0.5$ with the same circuit parameters. For the 2L-DAB converter, the optimized modulation methods to minimize rms current in [14] and [19] are used; meanwhile, the modulation method proposed in this article are employed in the NH3L-DAB. The circuit parameters for both

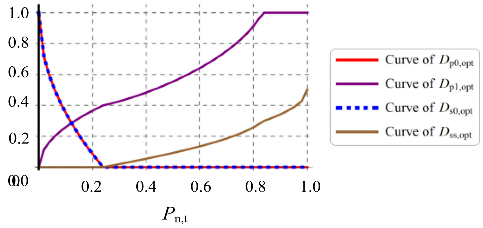

Fig. 24. Trajectories of optimal control variables versus transmitted power in the case $0.5 < M \leq 1$ ($M = 0.7$).

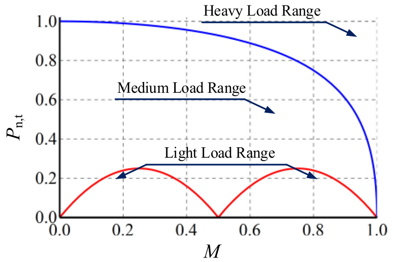

Fig. 25. Ranges of three kinds of load patterns.

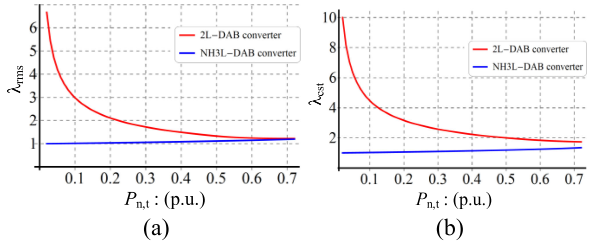

Fig. 26. Comparisons of NH3L-DAB and 2L-DAB at M = 0.5. (a) λ_{rms}. (b) λ_{cst}.

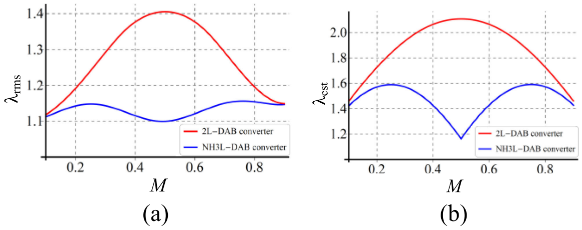

Fig. 27. Comparisons of NH3L-DAB and 2L-DAB of forward operation at $P_{\text{n,t}} = 0.45$. (a) λ_{rms}. (b) λ_{cst}.

TABLE V

OPTIMAL MODULATION METHOD FOR $M > 1$ CONDITION

Load Pattern	Optimal Modulation Strategy
Light Load pattern	$D_{p0,opt} = 1 + MD_{s0,opt} - M$ $D_{ss,opt} = 0$ $D_{p1,opt} = 1 - D_{p0,opt}$
Medium Load Pattern	$D_{p0,opt} = 0$ $D_{p1,opt} = 1$ $D_{ss,opt} = \frac{1 - D_{s0,opt} - M + MD_{s0,opt}}{2} + \frac{\sqrt{D_{s0,opt}^2 - 1 + M^2\left(1 - D_{s0,opt}\right)^2}}{2}$
Heavy Load Pattern	$D_{p0,opt} = 0$ $D_{p1,opt} = 1$ $D_{s0,opt} = 0$

topologies are the same: $v_1 = 400$ V, $v_2 = 20$ V, $N = 10$, $L_{\text{s}} = 20\,\mu$H, and $f_{\text{s}} = 160$ kHz. The red lines in both figures depict λ_{rms} and λ_{cst} for the case of 2L-DAB. As the figures show, λ_{rms} and λ_{cst} of the NH3L-DAB is much smaller than those of 2L-DAB converter for the whole operating range. For instance, at $P_{\text{n,t}} = 0.45$, the NH3L-DAB converter achieves 26.3% reduction of λ_{rms} and 41.1% λ_{cst} reduction. The smaller λ_{rms} implies less conduction loss, and the smaller λ_{cst} means less switching loss. Therefore, NH3L-DAB can achieve much higher efficiency in contrast with the conventional 2L-DAB converter.

Furthermore, when M varies from 0 to 1, the comparisons of λ_{rms} and λ_{cst} for both NH3L-DAB and 2L-DAB are illustrated in Fig. 27 with $P_{\text{n,t}} = 0.45$. In this case, both NH3L-DAB and 2L-DAB use the corresponding minimum rms current modulations. As the figures show, NH3L-DAB converter has less conduction losses and current stress at most operating points, especially when M is around 0.5. Moreover, the distribution of rms current and current stress of NH3L-DAB has less variation. It makes NH3L-DAB have better performance within the whole voltage range.

E. Modulation Optimization for 1 < M

When M is larger than 1, indicating $N \times v_2 > v_1$, NH3L-DAB converter works in boost condition. By investigating the GOC equation, it can be found that the optimal control coordinates are the same as the optimal schemes for the 2L-DAB converter [19], which are listed in Table V. Hence, we will not discuss this case further.

V. OPTIMAL MODULATION SCHEME FOR MINIMIZING THE RMS VALUE OF INDUCTOR CURRENT IN REVERSE OPERATION

Similar to the forward operation, the control coordinates $\boldsymbol{D}_{\text{opt}}$ that can minimize the conduction losses for given p_{set} and M can be derived by solving the GOC equation (8). As shown in Fig. 5, there are two matching points for the input and output voltage, i.e., $v_1/2 = N \times v_2$ and $v_1 = N \times v_2$. In terms of M, three cases will be discussed separately, i.e., $0 \leq M < 1$, $1 \leq M \leq 2$, and $M > 2$. By calculating and analyzing ξ_{Dx} for each operating mode,

$$\begin{cases} i_L\left(0\right) = i_L\left(D_{\text{p0}}T\right) = -\left(1 + D_{\text{p1}} + M\left(4D_{\text{ss}} - 2\right)\right) \times \frac{v_1 T}{4L_{\text{s}}} \\ i_L\left(D_{\text{ss}}T\right) = i_L\left(\left(D_{\text{ss}} + D_{\text{s0}}\right)T\right) = -\left(D_{\text{p1}} + 1 - 4D_{\text{ss}} - 2M\right) \times \frac{v_1 T}{4L_{\text{s}}} \\ i_L\left(\left(D_{\text{p0}} + D_{\text{p1}}\right)T\right) = \left(D_{\text{p1}}\left(3 - 4M\right) + M\left(4D_{\text{ss}} + 2\right) - 1\right) \times \frac{v_1 T}{4L_{\text{s}}} \end{cases} \qquad (27)$$

TABLE VI
THREE COMMON MODES WITH DEFINITION DOMAIN AND POWER TRANSMISSION FUNCTIONS

Mode	Definition Domain	Power Transmission
1	$-1+D_{p0}+D_p \le D_{s0}$ $+D_{ss} \le 0 \le D_{p0} \le D_{p0}$ $+D_p \le 1+D_{ss} \le 1$	$P_{M1}=\frac{Nv_1v_2T}{4L_s}\times\begin{pmatrix}D_p\left(-D_p-2D_{p0}+D_{s0}+2D_{ss}+1\right)\\2D_{p0}\left(-D_{p0}+D_{s0}+2D_{ss}+1\right)\\-2D_{s0}\left(D_{s0}+2D_{ss}+1\right)-4D_{ss}^2-4D_{ss}\end{pmatrix}$
2	$-1+D_{p0} \le D_{s0}+D_{ss} \le$ $-1+D_{p0}+D_p \le 0 \le D_{p0}$ $\le 1+D_{ss} \le D_{p0}+D_p \le 1$	$P_{M2}=\frac{Nv_1v_2T}{4L_s}\times\begin{pmatrix}2D_pD_{p0}-2D_{p0}-3D_p-D_pD_{s0}\\+2D_pD_{ss}+2D_{s0}D_{ss}+D_p^2-D_{s0}^2\\-2D_{ss}^2+2\end{pmatrix}$
3	$0 \le D_{p0} \le D_{s0}+D_{ss} \le$ $1+D_{ss} \le D_{p0}+D_p \le 1$	$P_{M3}=\frac{Nv_1v_2T}{4L_s}\times\begin{pmatrix}D_pD_{s0}-2D_{s0}-2D_{ss}\\-D_p+2D_{s0}D_{ss}+D_{s0}^2+1\end{pmatrix}$

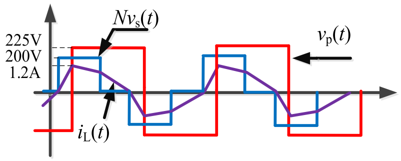

Fig. 28. Typical waveforms of NH3L-DAB converter with the modulation scheme in (28) for Mode 2 ($P_{n,t} = 0.06$ and $v_1 = 450$ V).

it can be concluded that all the optimal control coordinates $\boldsymbol{D}_{\rm opt}$ are located in Mode 1, Mode 2, and Mode 3 when $M > 1$. The definition domain and power transmission functions of Modes 1–3 are presented in Table VI, and the relevant analysis of all modes is presented in Table X in the Appendix.

A. Modulation Optimization for 2 < M

By considering the definition of Mode 2, the effective solution of the GOC equation is expressed as follows:

$$\begin{aligned}D_{\rm p,opt} &= 1\\ D_{\rm p0,opt} &= 0\\ D_{\rm s0,opt} &= \tfrac{(2D_{\rm ss,opt}+1)(M-2)}{2-2M}.\end{aligned} \tag{28}$$

In the domain of Mode 2, the range of $D_{\rm s0}$ is $[0, -D_{\rm ss}]$, and the range of $D_{\rm ss}$ is $[-0.5, \frac{M-2}{2}]$. Based on the above analysis, the power range in this working condition is

$$\left[0, \frac{1}{2}\right]. \tag{29}$$

The power range of (29) can be regarded as the light load range; the current of the devices at each switching moment can be obtained as follows:

$$\begin{cases} i_L\left(0\right) = i_L\left(D_{\rm p0}T\right) = \left(-2D_{\rm s0} - 4D_{\rm ss} - 2 - M\right)\frac{v_2T}{L_{\rm s}}\\ i_L\left((1+D_{\rm ss})T\right) = \left((2-2D_{\rm s0}) + (-1-2D_{\rm ss})\,M\right)\frac{v_2T}{L_{\rm s}}\\ i_L\left((1+D_{\rm ss}+D_{\rm s0})T\right)\\ = \left((2-2D_{\rm s0}) + (-1-2D_{\rm ss}-2D_{\rm s0})\,M\right)\frac{v_2T}{L_{\rm s}}\\ i_L\left((D_p+D_{\rm p0})\right) = \left(2D_{\rm s0} - 4D_{\rm ss} + 2 - M\right)\frac{v_2T}{L_{\rm s}}\\ i_L\left(T\right) = \left(2D_{\rm s0} + 4D_{\rm ss} + 2 - M\right)\frac{v_2T}{L_{\rm s}}. \end{cases} \tag{30}$$

In this scenario, the prerequisite condition of ZVS for all switching devices is satisfied. Fig. 28 illustrates the operating waveforms for the optimal control coordinates in (28).

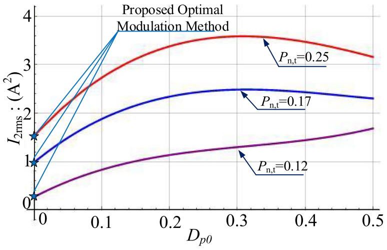

Fig. 29. Curves of $I_{2\rm rms}$ versus $D_{\rm p0}$ with different output power, $P_{\rm n,t}$.

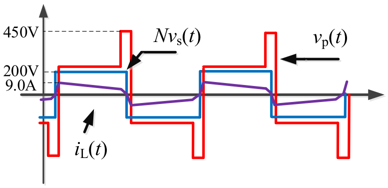

Fig. 30. Typical waveforms of NH3L-DAB converter with the modulation scheme for Mode 1 ($P_{\rm n,t} = 0.48$ and $v_1 = 450$ V).

The case of $M = 2.2$ is illustrated as an example. Fig. 29 shows the curves of $I_{2\rm rms}$ versus $D_{\rm p0}$ when the voltage matching condition is satisfied, and $P_{\rm n,t}$ remains constant for each curve. As Fig. 29 shows, the increment of $D_{\rm p0}$ leads to an increment of $I_{2\rm rms}$. Hence, the minimum value of $I_{2\rm rms}$ at voltage matching state is obtained at $D_{\rm p0} = 0$, i.e., the solutions of GOC equation, as shown in (28).

In medium load range scenario, by solving the GOC equation in Mode 1, the control coordinate for minimum $I_{2\rm rms}$ can be derived as

$$\begin{aligned} D_{\rm p,opt} &= 4D_{\rm ss,opt} - \frac{2}{M} + 2\\ D_{\rm p0,opt} &= D_{\rm s0,opt} = 0. \end{aligned} \tag{31}$$

Among them, the range of $D_{\rm p}$ is $[0, 1]$, and the range of $D_{\rm ss}$ is $[\frac{1-M}{2M}, \frac{2-M}{4M}]$. Then, replace $D_{\rm ss}$ in $P_{\rm n,t}$ for Mode 1, and we can get the power transmission range of Mode 1 is $P_{n,t} \in [\frac{1}{4} - \frac{1}{M^2}, 1 - \frac{1}{M^2}]$. The above power range is defined as medium load. Since there is an overlapping area in the power range of light load and medium load, the switching devices in the side of large current operate at ZCS condition in Mode 1, so the strategy of $\boldsymbol{D}_{\rm opt}$ in Mode 1 is preferred in the power overlapping area. The boundaries of light load and medium load are denoted as BC1 and BC2.

In this scenario, the prerequisite condition of the ZVS for S_1–S_6 is achieved; meanwhile, Q_1–Q_4 can achieve ZCS. Fig. 30 illustrates the operating waveforms for the optimal control coordinates.

In medium load range, the curved surface of $I_{2\rm rms}$ versus $D_{\rm s0}$ and $D_{\rm p0}$ is illustrated in Fig. 31. In this scenario, $P_{\rm n,t} = 0.15$, $M = 2.25$. As can be observed, $I_{2\rm rms}$ has a unique global minimum point. This verifies that the control method can minimize the current rms value.

When the transferred power is larger than $1 - \frac{1}{M^2}$, it is defined as the high load range. By analyzing the optimization equation, the modulation strategy of GOC in heavy load range is

$$D_{\rm s0,opt} = D_{\rm p,opt} = D_{\rm p0,opt} = 0. \tag{32}$$

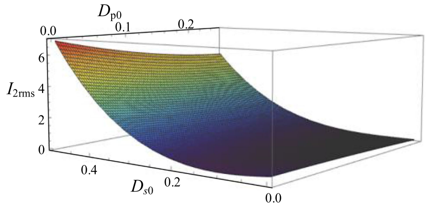

Fig. 31. Curved surface of $I_{2\mathrm{rms}}$ versus D_{p0} and D_{s0} when $P_{\mathrm{n,t}} = 0.15$ and $M = 2.25$.

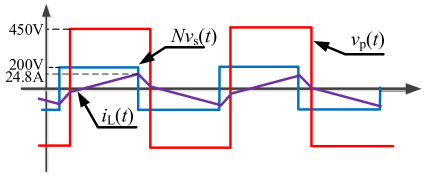

Fig. 32. Typical waveforms of NH3L-DAB converter with the modulation scheme for Mode 1 ($P_{\mathrm{n,t}} = 0.9$ and $v_1 = 450$ V).

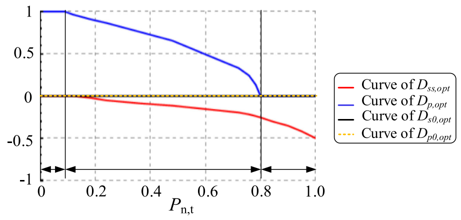

Fig. 33. Trajectories of optimal control variables versus transmitted power in the case $2 < M$ ($M = 2.25$).

In the heavy load range, only D_{ss} is used to adjust the output power, which is the same as the modulation strategy of high power with two-level SPS modulation. The corresponding range of transferred power and the control variable in this range are as follows:

$$\mathrm{P}_{\mathrm{n,t}} \in \left[1 - \frac{1}{M^2}, 1\right] \tag{33}$$

$$D_{\mathrm{ss}} \in \left[-\frac{1}{2}, -\frac{1 - M + \sqrt{M^2 - 1}}{2}\right]. \tag{34}$$

The power range of (33) is defined as the heavy load stage. The typical working waveform is shown in Fig. 32.

In the heavy load range, the inductor current at the switching moment of each device is given as follows:

$$\begin{cases} i_L\left(0\right) = i_L\left(D_{\mathrm{p0}}T\right) \\ \qquad = i_L\left((D_{\mathrm{p0}} + D_p)T\right) = \left(\left(-2D_{\mathrm{ss}} - 1\right) + M\right) \frac{v_2 T}{2L_{\mathrm{s}}} \\ i_L\left((1 + D_{\mathrm{ss}})T\right) = \left(1 - \left(2D_{\mathrm{ss}} + 1\right) M\right) \frac{v_2 T}{2L_{\mathrm{s}}} \\ i_L\left(T\right) = i_L\left((1{+}D_{\mathrm{ss}} + D_{\mathrm{s0}})\right) = \left(\left(2D_{\mathrm{ss}} + 1\right) - M\right) \frac{v_2 T}{2L_{\mathrm{s}}}. \end{cases} \tag{35}$$

Combining (28), (31), and (32), the closed-form solutions of $\boldsymbol{D}_{\mathrm{opt}}$ in the case of $2 \leq M$ are obtained. With given M, there is a unique solution $\boldsymbol{D}_{\mathrm{opt}}$ for each normalized transmitted power point. The trajectories of four control variables versus $P_{\mathrm{n,t}}$ are illustrated in Fig. 33 with $M = 2.25$.

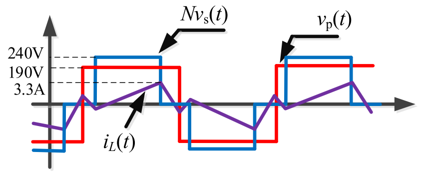

Fig. 34. Typical waveforms of NH3L-DAB converter with the modulation scheme in (36) ($P_{\mathrm{n,t}} = 0.08$ and $v_1 = 380$ V).

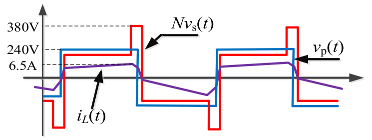

Fig. 35. Typical waveforms of NH3L-DAB converter with the modulation scheme in (38) ($P_{\mathrm{n,t}} = 0.35$ and $v_1 = 380$ V).

B. Modulation Optimization for 1 ≤ M ≤ 2

Considering the range of M, the optimization equation of GOC in the domain of Modes 2 and 3 is recalculated, and a set of general solutions can be obtained. The solution is defined as follows:

$$\begin{aligned} D_{\mathrm{p,opt}} &= 1 \\ D_{\mathrm{p0,opt}} &= 0 \\ D_{\mathrm{s0,opt}} &= \frac{\left(2D_{\mathrm{ss}}{+}1\right)\left(M - 2\right)}{2 - 2M}. \end{aligned} \tag{36}$$

Fig. 34 illustrates the operating waveforms for the optimal control coordinates in (36). The current of the inductor at each switching moment is given as

$$\begin{cases} i_L\left(0\right) = i_L\left(D_{\mathrm{p0}}T\right) = \left(\left(2D_{\mathrm{s0}} - 2\right) + M\right) \frac{v_2 T}{4L_{\mathrm{s}}} \\ i_L\left((D_{\mathrm{s0}} + D_{\mathrm{ss}})T\right) \\ = \left(\left(2D_{\mathrm{s0}} - 2\right) + \left(1 - 2D_{\mathrm{s0}} - 2D_{\mathrm{ss}}\right) M\right) \frac{v_2 T}{4L_{\mathrm{s}}} \\ i_L\left((1 + D_{\mathrm{ss}})T\right) = \left(\left(2 - 2D_{\mathrm{s0}}\right) + \left(-1 - 2D_{\mathrm{ss}}\right) M\right) \frac{v_2 T}{4L_{\mathrm{s}}} \\ i_L\left((D_p + D_{\mathrm{p0}})\right) = \left(\left(2 - 2D_{\mathrm{s0}}\right) - M\right) \frac{v_2 T}{4L_{\mathrm{s}}} \\ i_L\left(T\right) = -\left(\left(2D_{\mathrm{s0}} - 2\right) + M\right) \frac{v_2 T}{4L_{\mathrm{s}}}. \end{cases} \tag{37}$$

When the transferred power increases above the upper limit of Modes 2 and 3, the NH3L-DAB converter comes to the medium-load area and works in Mode 1. Analyzing the GOC equation in the defined domain of Mode 1, the optimal control strategy can be obtained as follows:

$$\begin{aligned} D_{\mathrm{p,opt}} &= 4D_{\mathrm{ss,opt}} - \frac{2}{M} + 2 \\ D_{\mathrm{p0,opt}} &= D_{\mathrm{s0,opt}} = 0. \end{aligned} \tag{38}$$

Fig. 35 illustrates the operating waveforms for the optimal control coordinates obtained by (38) and the current of the inductor at each switching moment is given as (39). The range of D_{ss} is $[\frac{1-M}{2M}, 0]$; therefore, the transferred power range of this working condition is $[\frac{6M-2M^2-4}{M^2}, \frac{M^2-1}{M^2}]$. The above power range is defined as medium load range. Since there is an overlap area in the power range of light load and medium load, the switching devices of the high current side operate at ZCS condition in Mode 1, so the proposed modulation of $\boldsymbol{D}_{\mathrm{opt}}$ for

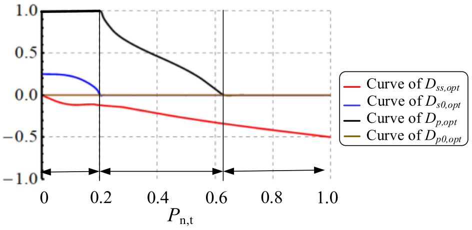

Fig. 36. Trajectories of optimal control variables versus transmitted power in the case $1 \leq M \leq 2$ ($M = 1.58$).

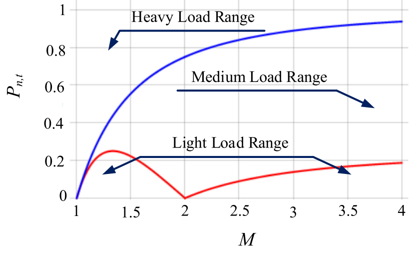

Fig. 37. Ranges of three kinds of load patterns when $M > 1$.

Mode 1 is preferred in the power overlap area. The light-load and medium-load boundaries are denoted as BD1 and BD2

$$\begin{cases} i_L\left(0\right) = i_L\left(D_{\text{p0}}T\right) = -D_{\text{ss}}\left(1+M\right)\frac{v_2 T}{L_{\text{s}}} \\ i_L\left((D_{\text{p0}}+D_{\text{p}})T\right) \\ = \left(-2M + \left(3D_{\text{ss}}+3\right) - M - 3D_{\text{ss}}M\right)\right)\frac{v_2 T}{L_{\text{s}}} \\ i_L\left((1+D_{\text{ss}})T\right) = i_L\left((1{+}D_{\text{ss}}+D_{\text{s0}})\right) = 0 \\ i_L\left(T\right) = D_{\text{ss}}\left(1+M\right)\frac{v_2 T}{L_{\text{s}}}. \end{cases} \quad (39)$$

Combining the expressions of (32), (36), and (38), the closed-form expressions of $\boldsymbol{D}_{\text{opt}}$ in the case of $1 \leq M \leq 2$ are obtained. And the trajectories of all four control variables ($D_{\text{p0,opt}}$, $D_{\text{p,opt}}$, $D_{\text{s0,opt}}$, $D_{\text{ss,opt}}$) versus $P_{\text{n,t}}$ are illustrated in Fig. 36 with $M = 1.58$ ($M = 1.58$ is selected as an example). In this scenario, $D_{\text{p0,opt}}$ is equal to 0 for all operating points.

As to the heavy load power range of $1 \leq M \leq 2$, the converter operates as a 2L-DAB converter. The typical waveform is shown in Fig. 32. Therefore, the optimized control scheme of the inductor current is the same as SPS modulation scheme of 2L-DAB converter that has been investigated comprehensively in the literature. Then, we will not go further to discuss this scenario.

For the cases of $M > 2$ and $1 \leq M \leq 2$, the prerequisite condition of ZVS for all devices in the whole power range for the application of reverse power flow is met based on Table II.

C. Synthesis of the Optimal Modulation Method

In Fig. 37, curves of the light load, medium load, and heavy load versus M are illustrated. These three load patterns cover the whole power range of NH3L-DAB without overlapping or vacancy. The light load range is much smaller than 2L-DAB, and the medium load range is enlarged significantly. When M is equal to 2, the range of light load is 0, NH3L-DAB converter mainly operates at medium load range.

Fig. 38 illustrates the comparisons of λ_{rms} and λ_{cst} of NH3L-DAB and that of conventional 2L-DAB at $M = 2$ with the same circuit parameters. For the 2L-DAB converter, the optimized modulation methods to minimize rms current in [14] and [19] are used; meanwhile, the modulation method proposed in this article is employed in the NH3L-DAB. The circuit parameters for both topologies are the same: $v_2 = 20$ V, $v_1 = 400$ V, $N = 10$, $L_{\text{s}} = 20\,\mu$H, and $f_{\text{s}} = 160$ kHz. The red lines in both figures depict λ_{rms} and λ_{cst} for the case of 2L-DAB. As the figures show, λ_{rms} and λ_{cst} of NH3L-DAB converter are much smaller than those of 2L-DAB converter for the whole operating range. For instance, at $P_{\text{n,t}} = 0.4$, NH3L-DAB converter achieves 32.7% reduction of λ_{rms} and 62.9% reduction of λ_{cst}. The smaller λ_{rms} implies less conduction loss, and the smaller λ_{cst} means less switching loss. Therefore, NH3L-DAB can achieve much higher efficiency in contrast with the conventional 2L-DAB converter.

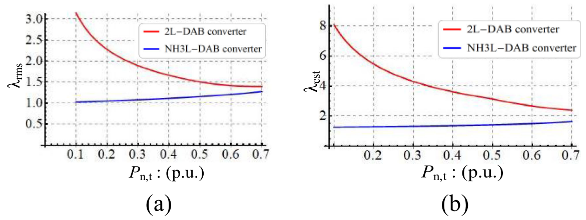

Fig. 38. Comparisons of NH3L-DAB and 2L-DAB at $M = 2$. (a) λ_{rms}. (b) λ_{cst}.

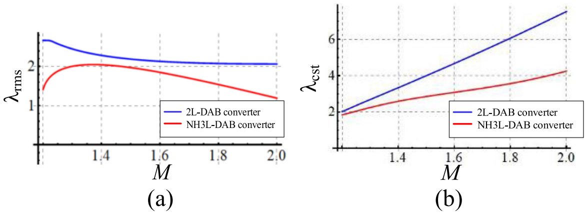

Fig. 39. Comparisons of NH3L-DAB and 2L-DAB of reverse operation at $P_{\text{n,t}} = 0.45$. (a) λ_{rms}. (b) λ_{cst}.

Furthermore, when M varies from 1 to 2, the comparisons of λ_{rms} and λ_{cst} for both NH3L-DAB and 2L-DAB converters are illustrated in Fig. 39 with $P_{\text{n,t}} = 0.45$. In this case, both NH3L-DAB and 2L-DAB converters use the corresponding modulations of minimum rms current. As the figures show, NH3L-DAB converter has less conduction losses and current stress. Moreover, the distribution of rms current and current stress of NH3L-DAB has less variation. It makes NH3L-DAB have better performance within the whole voltage range.

D. Modulation Optimization for $0 \leq \mathrm{M} < 1$

In forward mode, when M is less than 1, indicating $Nv_2 < v_1$, NH3L-DAB converter is working in buck mode. However, NH3L-DAB is a boost converter connected with a DAB converter when operating in reverse mode. The voltage level of $\pm v_1/2$ cannot be generated; therefore, the converter works in the two-level mode, i.e., $\pm v_1$. By investigating the GOC equation, it can be found that the optimal control coordinates are the same as the optimal schemes for the 2L-DAB converter [19], which are listed in Table VII.

Based on the above analysis of the bidirectional optimized modulation strategy, the closed-loop control method of NH3L-DAB is obtained as shown in Fig. 40, where v_1 represents the voltage in HV side, and v_2 represents the voltage in the LV side.

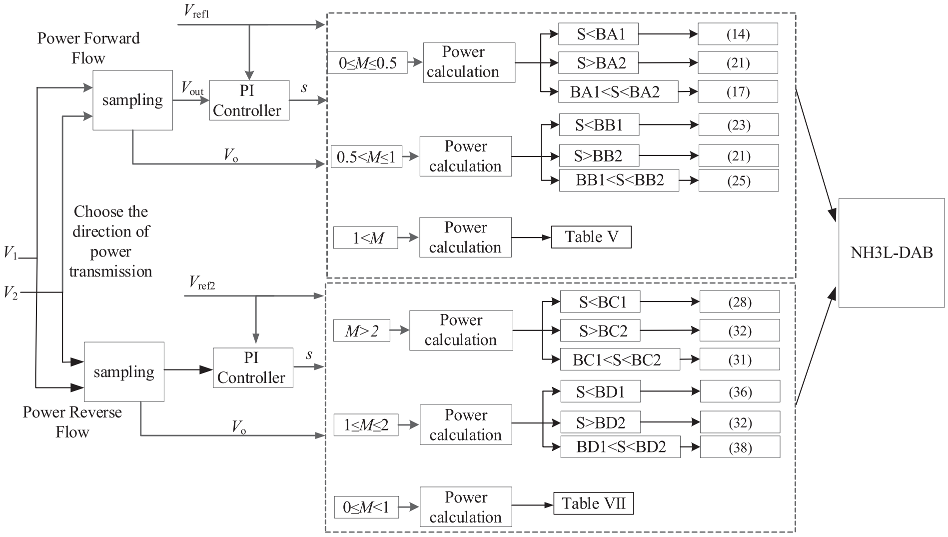

Fig. 40. Closed-loop control block diagram of NH3L-DAB.

TABLE VII
OPTIMAL MODULATION METHOD FOR $M < 1$ CONDITION

Load Pattern	Optimal Modulation Strategy
Light Load pattern	$D_{p0,opt}=1-\frac{1-D_{s0,opt}}{M}$ $D_{ss,opt}=\frac{(1-M)(1-D_{s0,opt})}{M}$ $D_{p,opt}=0$
Medium Load Pattern	$D_{p0,opt}=D_{p,opt}=0$ $D_{ss,opt}=\frac{D_{s0,opt}-1+M+MD_{s0,opt}}{2M}+\frac{\sqrt{(D_{s0,opt}-1)^2+M^2(D_{s0,opt}^2-1)}}{2M}$
Heavy Load Pattern	$D_{p0,opt}=D_{p,opt}=D_{s0,opt}=0$

TABLE VIII
CIRCUIT PARAMETERS OF THE NH3L-DAB PROTOTYPE

Items	Descriptions	Specifications
v_1	High Voltage	200V-450V
v_2	Low Voltage	20V-28.8V
f_s	Switching Frequency	160kHz
L_s	Leakage inductor	20.8μH
N	Turns Ratio	10:1
	Magnetic Material	Ferrite
S_1-S_6	Primary switching devices	GS66508T(GaN System)
D_1-D_2	Clamped Diode	C3D10065E (Cree)
Q_1-Q_4	Secondary switching devices	BSC014N04 (Infineon)
	Controller	TMS320F28379D (TI)

VI. EXPERIMENTAL VERIFICATION

In order to demonstrate the effectiveness of three-level architecture and the proposed modulation method, a prototype of NH3L-DAB converter with 200–450 V in HV side and 20–28.8 V in LV side is built. The high-frequency transformer consists of two transformers that are series connected in HV side and parallel connected in LV side. The sum of leakage inductor L_s of these two transformers is 20.8 μH and L_s has been integrated into the transformer to improve the power density. The specifications of the prototype are listed in Table VIII, and the photographs of the prototype are shown in Figs. 41 and 42.

A. Experimental Results for Forward Mode

In order to verify the superiority of the proposed solution for wide voltage application, 12 different conditions of NH3L-DAB prototype have been tested in the forward mode: the input voltage at 200, 300, 380, and 450 V; meanwhile, the corresponding output voltage at 20, 24, and 28.8 V. In each condition, the

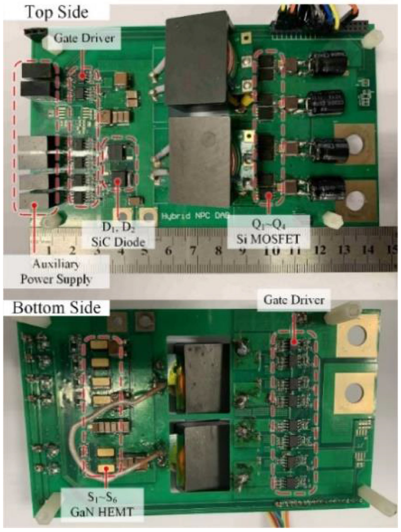

Fig. 41. Photograph of the NH3L-DAB converter prototype.

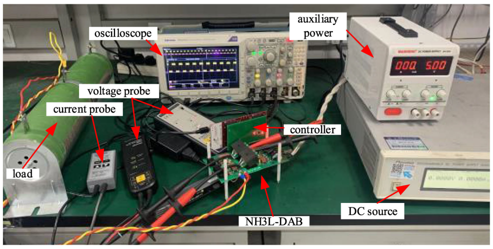

Fig. 42. Experimental system of the NH3L-DAB converter prototype.

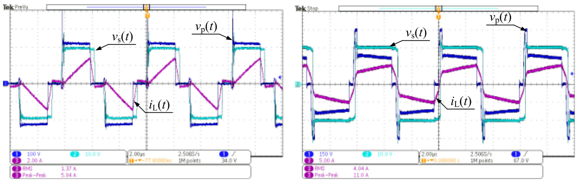

(a) (b)

Fig. 43. Experimental waveforms at $v_1 = 450$ V and $v_2 = 20$ V. (a) 10 A output current for light load. (b) 40 A output current for medium load.

output current ranges from 10 to 40 A, and the proposed optimal modulation method is employed at all operating points. The following three conditions are taken as the examples and mainly discussed: $v_1 = 450$ V and $v_2 = 20$ V for $M \leq 0.5$; $v_1 = 380$ V and $v_2 = 24$ V for $0.5 < M \leq 1$; $v_1 = 200$ V and $v_2 = 28.8$ V for $1 < M$.

1) $v_1 = 450$ V and $v_2 = 20$ V With M = 0.44: Fig. 43 shows the experimental waveforms with $v_1 = 450$ V and $v_2 = 20$ V by applying the proposed optimal modulation. Accordingly, the ranges of $P_{\mathrm{n,t}}$ for light load and medium load are [0, 0.11] and [0.11, 0.95], respectively. For the light load pattern, the experimental waveforms are shown in Fig. 43(a) when the output current is 10 A with $P_{\mathrm{n,t}} = 0.057$. As the theoretical analysis shown in Section IV, $i_L(t)$ is triangular wave, and v_{p}(t) has only the voltage levels 0 and $\pm v_1$ /2. Although the rms current has been reduced to 1.37 A in Fig. 43(a), the efficiency is tested to be 87.84%. It should be pointed out that the loss is mainly caused by the relatively large switching losses at HV side with an extremely light load. When S_2, S_3, S_5, and S_6 are turned ON, the inductor current $i_L(t)$ is almost 0, and ZVS cannot be completely realized. While S_1 needs to realize ZVS completely, according to [45], the current value should be $i_L(S_{1,\text{ on}})<–0.94$ A. In the experiment, the current value when S_1 is turned ON is –3 A, so S_1 can achieve complete ZVS, and S_4 has a similar conclusion. The similar method in [15] for 2L-DAB converter can also be used to develop ZVS modulation for NH3L-DAB converter based on the minimum rms current modulation strategies in this article. In Fig. 43(b), the experimental waveforms are shown when the output current is 40 A, and then, NH3L-DAB converter goes into the medium load pattern. When considering the junction capacitance of GaN devices, while S_1 and S_2 need to realize ZVS completely, the current value should satisfy $i_L(S_1/S_{2,\text{ on}})<–0.77$ A. Similarly, when S_6 needs to realize ZVS completely, the condition of $i_L(S_{6,\mathrm{on}}) < 0$ A should be satisfied. In the experimental results of above power condition, the current values when S_1 and S_6 are turned ON are –7.2 and –1.5 A, respectively, so complete ZVS operation can be achieved. Please note that ZVS of S_3 is incomplete as $i_L(t)$ may discharge the junction capacitor of S_3 and S_4 from $v_1/2$ to $v_1/4$ simultaneously when S_1 is turned OFF. This problem can be solved by using the active neutral point clamping (ANPC) method [39], [40]. Then, D_1 and D_2 of the clamping diodes in Fig. 1 are replaced by two active switching devices. Due to the realization of the soft switching in more devices in medium load, the conversion efficiency is up to 95.32%. However, with respect to the medium voltage level $\pm v_1/2$, the current should flow through the SiC Schottky diodes whose voltage drop is relatively large, leading to the additional losses. Therefore, the efficiency of this load pattern can be improved further by using the ANPC structure.

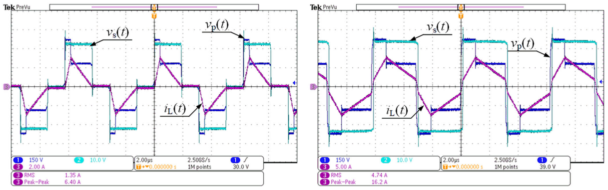

(a) (b)

Fig. 44. Experimental waveforms at $v_1 = 380$ V and $v_2 = 24$ V. (a) 10 A output current for light load. (b) 40 A output current for medium load.

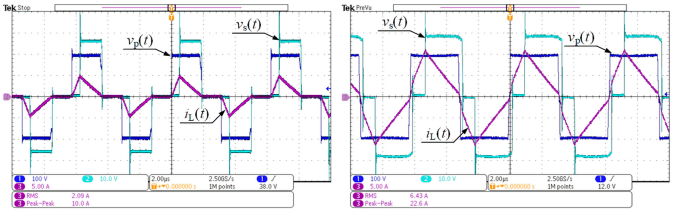

(a) (b)

Fig. 45. Experimental waveforms at $v_1 = 200$ V and $v_2 = 28.8$ V. (a) 10 A output current for light load. (b) 40 A output current for medium load.

2) $v_1 = 380$ V and $v_2 = 24$ V With M = 0.63: In the case of $v_1 = 380$ V and $v_2 = 24$ V, the operating waveforms are illustrated in Fig. 44 by using the proposed optimal modulation. Accordingly, the ranges of $P_{\mathrm{n,t}}$ for light load and medium load are [0, 0.19] and [0.19, 0.87], respectively. Fig. 44(a) shows the experimental results with 10 A output current at light load pattern. Compared with the condition of $M \leq 0.5$, the duty ratio for $\pm v_1$ voltage level in this scenario does not equal to 0. The conversion efficiency is tested to be 91.4%. When the output current is up to 40 A, as in Fig. 44(b), NH3L-DAB converter is working at medium voltage pattern. Then, the switching losses have been significantly reduced by achieving ZVS at HV side, and the efficiency goes to 95.72%.

3) $v_1 = 200$ V and $v_2 = 28.8$ V With M = 1.44: For the voltage condition of $1 < M$, Fig. 45 shows the experimental waveforms with $v_1 = 200$ V and $v_2 = 28.8$ V by applying the proposed optimization modulation. Fig. 45(a) and (b) shows the waveforms for 10 and 40 A output, respectively. At light load point, since the input voltage is only 200 V, the switching losses of primary side H_1 caused by hard-switching are smaller than that of $v_1 = 380$ V or $v_1 = 450$ V, and the conversion efficiency is 93.05%. However, in medium load range, the efficiency is 92.73% due to the large turned-OFF losses at the secondary side H_2.

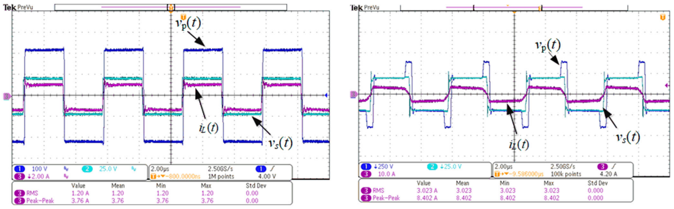

(a) (b)

Fig. 46. Experimental waveforms at $v_2 = 20$ V and $v_1 = 450$ V. (a) 10 A input current for light load. (b) 40 A input current for medium load.

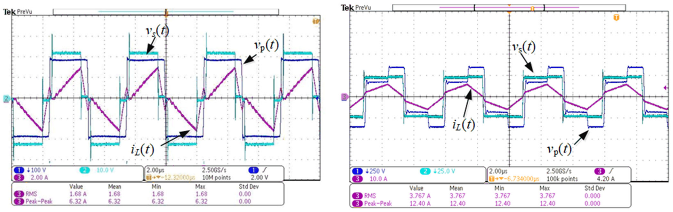

(a) (b)

Fig. 47. Experimental waveforms at $v_2 = 24$ V and $v_1 = 380$ V. (a) 10 A input current for light load. (b) 40 A input current for medium load.

B. Experimental Results for Reverse Mode

When the converter works in reverse mode, the corresponding input voltages are 20, 24, and 28.8 V. In each condition, the input current ranges from 10 to 40 A, and the proposed optimal modulation method is employed at all operating points. The following three conditions are taken as the examples and mainly discussed: $v_1 = 450$ V and $v_2 = 20$ V for $2 < M$; $v_1 = 380$ V and $v_2 = 24$ V for $1 \leq M \leq 2$; $v_1 = 200$ V and $v_2 = 28.8$ V for $M < 1$.

1) $v_2 = 20$ V and $v_1 = 450$ V With M $= 2.25$: Fig. 46 shows the experimental results of $v_2 = 20$ V and $v_1 = 450$ V. Accordingly, the ranges of $P_{\mathrm{n,t}}$ for light load and medium load are [0, 0.05] and [0.05, 0.8], respectively. Fig. 46(a) shows the waveform of the converter when the input current at LV side is 10 A and the converter works in low power. $i_L(t)$ is a triangular wave. Due to the optimized strategy, the rms value of the inductor current is reduced to 1.15 A, and the switching devices of HV side operate at ZVS condition and the switching devices in LV side operate at ZCS condition, the efficiency reached to 91.2%. In Fig. 46(b), the input current is increased to 40 A and the converter works in medium power range, the duty ratio of v_1 level is increased, and the efficiency is up to 94.73%.

2) $v_2 = 24$ V and $v_1 = 380$ V With M $= 1.538$: Fig. 47 shows the working conditions of $v_2 = 24$ V and $v_1 = 380$ V. Accordingly, the ranges of $P_{\mathrm{n,t}}$ for light load and medium load are [0, 0.19] and [0.19, 0.6], respectively. Fig. 47(a) shows the experimental results with 10 A input current at light load pattern. In this stage, all the switching devices operate at ZVS condition; however, the final efficiency of this method with little backflow power is tested to be 90.7% due to the large turn-OFF losses in the large current side. Fig. 47(b) shows the operating waveforms with 40 A input current at medium load pattern, and the backflow power is eliminated. The switching devices in HV side operate at ZVS condition and the switching devices in LV side operate at ZCS condition, and the efficiency is increased to 94.92%.

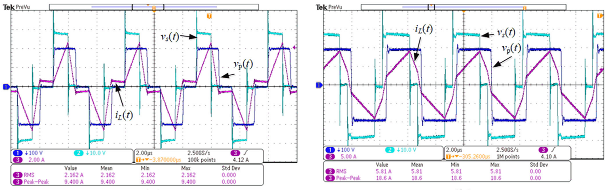

(a) (b)

Fig. 48. Experimental waveforms at $v_2 = 28.8$ V and $v_1 = 200$ V. (a) 10 A input current for light load. (b) 40 A input current for medium load.

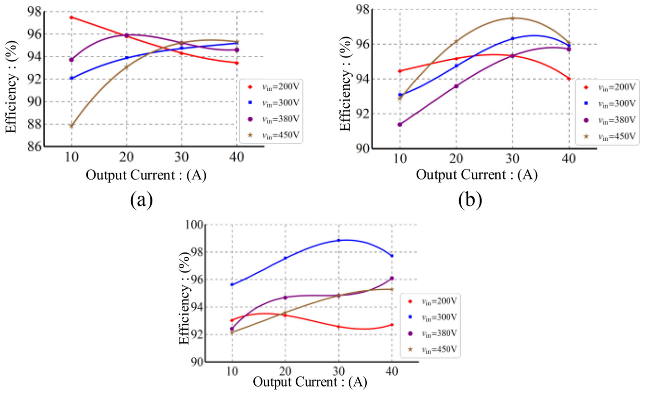

(a) (b)

(c)

Fig. 49. Efficiency comparisons at different voltage conditions of forward operation. (a) $v_2 = 20$ V. (b) $v_2 = 24$ V. (c) $v_2 = 28.8$ V.

3) $v_2 = 28.8$ V and $v_1 = 200$ V With M $= 0.694$: For the voltage condition of $M < 1$, Fig. 48 shows the experimental waveforms with $v_2 = 28.8$ V and $v_1 = 200$ V, and the currents are 10 and 40 A in the LV input side, respectively. At light load point, the switching devices S_5, S_6, Q_3, and Q_4 operate at hard-switching condition. Since the output voltage is only 200 V, the conversion efficiency is 90.05% due to the large switching losses. However, in medium load range, all of the switching devices operate at ZVS, and the efficiency is increased to 93.73%.

C. Synthesis of Experimental Results

The efficiency curves, which are obtained by fitting of the second-order interpolation function using the efficiency measurement of experiment at all test points, are shown in Fig. 49. In each subfigure, the output voltage is fixed; meanwhile, four curves are given for $v_1 = 200$ V, $v_1 = 300$ V, $v_1 = 380$ V, and $v_1 = 450$ V. The peak efficiency is 98.84% when the input voltage is 300 V and output voltage is 28.8 V ($M = 0.96$) with 30 A output. Moreover, in the case of $v_1 = 200$ V and $v_2 = 20$ V, the conversion efficiency decreases with the increase of output power, it is mainly caused by the turned-OFF losses of Q_1–Q_4, which increases significantly with the output current increases. For the same reason, in the case of $v_1 = 380$ V and $v_2 = 20$ V, the efficiency at 40 A output is also lower than the efficiency at 20 A output current. From another point of view, the efficiencies of the 12 operating conditions with 40 A output are compared with each other in Fig. 50. As the figure shows, when M increases from 0.44 to 1.44, the efficiency of most voltage range is higher than 94%. Therefore, it is demonstrated that NH3L-DAB converter and the proposed modulation method can be a good solution for the wide voltage range applications.

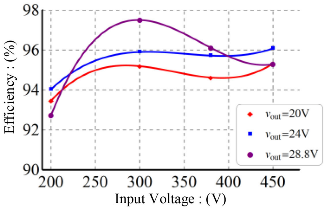

Fig. 50. Efficiency comparisons at 40 A output of forward operation.

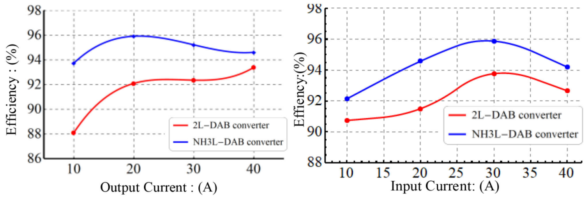

(a) (b)

Fig. 51. (a) Efficiency comparisons of NH3L-DAB converter and conventional 2L-DAB converter with $v_1 = 380$ V and $v_2 = 20$ V for forward operation. (b) Efficiency comparisons of NH3L-DAB converter and conventional 2L-DAB converter with $v_2 = 20$ V and $v_1 = 450$ V for reverse operation.

Furthermore, Fig. 51(a) shows the comparisons of the efficiency curve of NH3L-DAB to that of 2L-DAB at $v_1 = 380$ V and $v_2 = 20$ V. In order to achieve fair comparison, 2L-DAB also uses the components and the circuit parameters listed in Table VIII. According to the results shown in Fig. 51, NH3L-DAB converter can achieve higher efficiency than 2L-DAB converter of the full power range.

Fig. 51(b) shows the comparisons of the efficiency curve of NH3L-DAB to that of 2L-DAB at $v_2 = 20$ V and $v_1 = 450$ V of reverse operation. According to the results shown in Fig. 51(b), NH3L-DAB converter also can achieve higher efficiency than 2L-DAB converter of the full power range when works in reverse mode. Hence, the superior performance of NH3L-DAB converter is demonstrated.

In the experimental platform, the closed-loop block diagram in Fig. 40 is implemented in the microcontroller unit (MCU) program in real time. The executive time of the interrupt program is about 4.5 μs, and the switching cycle is 6.25 μs, and no additional memory is needed. Hence, the proposed controller for NH3L-DAB is practical solution for the application of wide voltage regulation.

VII. CONCLUSION

In the wide voltage range applications, multilevel DAB converters are the promising solutions to break the performance barriers of the state of the art for 2L-DAB converter. These improvements mainly originate from shaping the inductor current with better flexibility. Since only two additional switching devices are needed by NH3L-DAB converter, this very topology can achieve good balance between superior performance and cost-efficiency.

After investigating the operating principle of NH3L-DAB converter, this article derived the analytical solutions for the control variables (D_{p1}, D_{p0}, D_{s0}, D_{ss}) of a proposed optimal modulation scheme in forward mode and reverse mode, which can minimize the rms value of inductor current. Furthermore, the comparisons of theoretical calculation and experimental measurements between NH3L-DAB and 2L-DAB demonstrate that the three-level structure with the proposed modulation method help to facilitate efficiency improvement and significant reduction of current stress and conduction losses. Therefore, NH3L-DAB topology and the proposed modulation strategy can be a promising solution for the wide voltage range applications.

APPENDIX

TABLE IX
DEFINITION DOMAIN, POWER TRANSMISSION FUNCTIONS, AND POWER RANGE FOR EACH FORWARD OPERATING MODE (SIX COMMONLY USED MODES)

Mode	Definition domain and power transmission function	Power range
Mode 1	Definition domain: $0 \le D_{\mathrm{ss}} \le D_{\mathrm{ss}} + D_{\mathrm{s0}} \le D_{\mathrm{p0}} \le D_{\mathrm{p0}} + D_{\mathrm{p1}} \le 1$ $P_{M1} = \frac{N v_1 v_2 T}{4L_s} \times \begin{pmatrix} D_{\mathrm{p0}}^2 - D_{\mathrm{p1}}^2 + D_{\mathrm{s0}} + 2D_{\mathrm{ss}} + D_{\mathrm{p1}}\left(1 + D_{\mathrm{s0}} + 2D_{\mathrm{ss}}\right) \\ -D_{\mathrm{p0}}\left(1 + 2D_{\mathrm{p1}} + D_{\mathrm{s0}} + 2D_{\mathrm{ss}}\right) \end{pmatrix}$	Minimum $P_{\mathrm{n,t}} = -\frac{1}{2}$ at $\boldsymbol{D} = \left(\frac{1}{2}, \frac{1}{2}, 0, 0\right)$ Maximum $P_{\mathrm{n,t}} = \frac{1}{2}$ at $\boldsymbol{D} = \left(\frac{1}{2}, \frac{1}{2}, 0, \frac{1}{2}\right)$
Mode 2	Definition domain: $0 \le D_{\mathrm{ss}} \le D_{\mathrm{p0}} \le D_{\mathrm{ss}} + D_{\mathrm{s0}} \le D_{\mathrm{p0}} + D_{\mathrm{p1}} \le 1$ $P_{M2} = -\frac{N v_1 v_2 T}{4L_s} \times \begin{pmatrix} D_{\mathrm{p0}}^2 + D_{\mathrm{p1}}^2 - D_{\mathrm{s0}} + 2D_{\mathrm{s0}}^2 + 4D_{\mathrm{s0}}D_{\mathrm{ss}} + 2D_{\mathrm{ss}}^2 \\ +D_{\mathrm{p0}}\left(1 + 2D_{\mathrm{p1}} - 3D_{\mathrm{s0}} - 2D_{\mathrm{ss}}\right) \\ -2D_{\mathrm{ss}} - D_{\mathrm{p1}}\left(1 + D_{\mathrm{s0}} + 2D_{\mathrm{ss}}\right) \end{pmatrix}$	Minimum $P_{\mathrm{n,t}} = 0$ at $\boldsymbol{D} = (1, 0, 0, 0)$ Maximum $P_{\mathrm{n,t}} = \frac{2}{3}$ at $\boldsymbol{D} = \left(\frac{2}{3}, \frac{1}{3}, \frac{1}{3}, \frac{1}{3}\right)$
Mode 3	Definition domain: $0 \le D_{\mathrm{ss}} \le D_{\mathrm{p0}} \le D_{\mathrm{p0}} + D_{\mathrm{p1}} \le D_{\mathrm{ss}} + D_{\mathrm{s0}} \le 1$ $P_{M3} = \frac{N v_1 v_2 T}{4L_s} \times \begin{pmatrix} -D_{\mathrm{p0}} + D_{\mathrm{p1}}\left(1 - D_{\mathrm{s0}}\right) + D_{\mathrm{s0}} + D_{\mathrm{p0}}D_{\mathrm{s0}} \\ -D_{\mathrm{s0}}^2 + 2D_{\mathrm{ss}} - 2D_{\mathrm{s0}}D_{\mathrm{ss}} - D_{\mathrm{ss}}^2 \end{pmatrix}$	Minimum $P_{\mathrm{n,t}} = 0$ at $\boldsymbol{D} = \left(0, 1, \frac{1}{2}, \frac{1}{2}\right)$ Maximum $P_{\mathrm{n,t}} = \frac{4}{7}$ at $\boldsymbol{D} = \left(\frac{3}{7}, \frac{2}{7}, \frac{3}{7}, \frac{2}{7}\right)$
Mode 4	Definition domain: $0 \le D_{\mathrm{p0}} \le D_{\mathrm{ss}} \le D_{\mathrm{ss}} + D_{\mathrm{s0}} \le D_{\mathrm{p0}} + D_{\mathrm{p1}} \le 1$ $P_{M4} = \frac{N v_1 v_2 T}{4L_s} \times \begin{pmatrix} -3D_{\mathrm{p0}}^2 - D_{\mathrm{p1}}^2 + D_{\mathrm{s0}} - 2D_{\mathrm{s0}}^2 + 2D_{\mathrm{ss}} \\ -D_{\mathrm{p0}}\left(1 + 2D_{\mathrm{p1}} - 3D_{\mathrm{s0}} - 6D_{\mathrm{ss}}\right) - 4D_{\mathrm{ss}}^2 \\ -4D_{\mathrm{s0}}D_{\mathrm{ss}} + D_{\mathrm{p1}}\left(1 + D_{\mathrm{s0}} + 2D_{\mathrm{ss}}\right) \end{pmatrix}$	Minimum $P_{\mathrm{n,t}} = 0$ at $\boldsymbol{D} = (1, 0, 1, 0)$ Maximum $P_{\mathrm{n,t}} = 1$ at $\boldsymbol{D} = \left(1, 0, 0, \frac{1}{2}\right)$
Mode 5	Definition domain: $0 \le D_{\mathrm{p0}} \le D_{\mathrm{ss}} \le D_{\mathrm{p0}} + D_{\mathrm{p1}} \le D_{\mathrm{ss}} + D_{\mathrm{s0}} \le 1$ $P_{M5} = \frac{N v_1 v_2 T}{4L_s} \times \begin{pmatrix} -2D_{\mathrm{p0}}^2 + D_{\mathrm{p1}}\left(1 - D_{\mathrm{s0}}\right) + D_{\mathrm{s0}} - D_{\mathrm{s0}}^2 + 2D_{\mathrm{ss}} \\ -2D_{\mathrm{s0}}D_{\mathrm{ss}} - 3D_{\mathrm{ss}}^2 - D_{\mathrm{p0}}\left(1 - D_{\mathrm{s0}} - 4D_{\mathrm{ss}}\right) \end{pmatrix}$	Minimum $P_{\mathrm{n,t}} = 0$ at $\boldsymbol{D} = (1, 0, 1, 0)$ Maximum $P_{\mathrm{n,t}} = \frac{4}{5}$ at $\boldsymbol{D} = \left(\frac{3}{5}, 0, \frac{1}{5}, \frac{2}{5}\right)$
Mode 6	Definition domain: $0 \le D_{\mathrm{p0}} \le D_{\mathrm{p0}} + D_{\mathrm{p1}} \le D_{\mathrm{ss}} \le D_{\mathrm{ss}} + D_{\mathrm{s0}} \le 1$ $P_{M6} = \frac{N v_1 v_2 T}{4L_s} \times \begin{pmatrix} D_{\mathrm{p1}}\left(1 - D_{\mathrm{s0}} - 2D_{\mathrm{ss}}\right) - D_{\mathrm{p0}}\left(1 - D_{\mathrm{s0}} - 2D_{\mathrm{ss}} - 2D_{\mathrm{p1}}\right) \\ -D_{\mathrm{p0}}^2 + D_{\mathrm{p1}}^2 + D_{\mathrm{s0}} - D_{\mathrm{s0}}^2 + 2D_{\mathrm{ss}} - 2D_{\mathrm{s0}}D_{\mathrm{ss}} - 2D_{\mathrm{ss}}^2 \end{pmatrix}$	Minimum $P_{\mathrm{n,t}} = 0$ at $\boldsymbol{D} = (0, 0, 1, 0)$ Maximum $P_{\mathrm{n,t}} = \frac{3}{4}$ at $\boldsymbol{D} = \left(\frac{1}{2}, 0, 0, \frac{1}{2}\right)$

TABLE X

Definition Domain, Power Transmission Functions, and Power Range for Each Reverse Operating Mode (Eight Commonly Used Modes)

Mode	Definition domain and power transmission function	Power range
Mode 1	Definition domain: $-1+D_{p0}+D_p \le D_{s0}+D_{ss} \le 0 \le D_{p0} \le D_{p0}+D_p \le 1+D_{ss} \le 1$ $P_{M1}=\frac{Nv_1v_2T}{4L_s}\times\begin{pmatrix}-D_p^2-2D_pD_{p0}+D_pD_{s0}+2D_pD_{ss}+D_p\\-2D_{p0}^2+2D_{p0}D_{s0}+4D_{p0}D_{ss}+2D_{p0}-2D_{s0}^2\\-4D_{ss}D_{s0}-2D_{s0}-4D_{ss}^2-4D_{ss}\end{pmatrix}$	Minimum $P_{n,t}=0$ at $\boldsymbol{D}=(1,0,0,0)$ Maximum $P_{\mathrm{n,t}}=1$ at $\boldsymbol{D}=\left(0,0,0,-\frac{1}{2}\right)$
Mode 2	Definition domain: $-1+D_{p0} \le D_{s0}+D_{ss} \le -1+D_{p0}+D_p \le 0 \le D_{p0} \le 1+D_{ss} \le D_{p0}+D_p \le 1$ $P_{M2}=\frac{Nv_1v_2T}{4L_s}\times\begin{pmatrix}2D_pD_{p0}-2D_{p0}-3D_p-D_pD_{s0}+2D_pD_{ss}\\+2D_{s0}D_{ss}+D_p^2-D_{s0}^2-2D_{ss}^2+2\end{pmatrix}$	Minimum $P_{n,t}=-\frac{3}{4}$ at $\boldsymbol{D}=\left(\frac{1}{2},\frac{1}{2},0,-\frac{1}{2}\right)$ Maximum $P_{n,t}=\frac{1}{2}$ at $\boldsymbol{D}=\left(0,\frac{1}{2},0,-\frac{1}{2}\right)$
Mode 3	Definition domain: $0 \le D_{p0} \le D_{s0}+D_{ss} \le 1+D_{ss} \le D_{p0}+D_p \le 1$ $P_{M3}=\frac{Nv_1v_2T}{4L_s}\times\left(D_pD_{s0}-2D_{s0}-2D_{ss}-D_p+2D_{s0}D_{ss}+D_{s0}^2+1\right)$	Minimum $P_{n,t}=-\frac{1}{8}$ at $\boldsymbol{D}=\left(\frac{3}{4},\frac{1}{4},\frac{1}{2},0\right)$ Maximum $P_{n,t}=\frac{1}{2}$ at $\boldsymbol{D}=\left(\frac{1}{2},0,\frac{1}{2},-\frac{1}{2}\right)$
Mode 4	Definition domain: $0 \le D_{p0} \le D_{p0}+D_p \le D_{s0}+D_{ss} \le 1+D_{ss} \le 1$ $P_{M4}=\frac{Nv_1v_2T}{4L_s}\times\begin{pmatrix}D_p+2D_{p0}-2D_{s0}-4D_{ss}-D_pD_{s0}\\-2D_{p0}D_{s0}+4D_{ss}D_{s0}+2D_{s0}^2\end{pmatrix}$	Minimum $P_{n,t}=-\frac{1}{2}$ at $\boldsymbol{D}=\left(0,0,\frac{1}{2},0\right)$ Maximum $P_{n,t}=\frac{1}{2}$ at $\boldsymbol{D}=\left(0,0,\frac{1}{2},-\frac{1}{2}\right)$
Mode 5	Definition domain: $0 \le D_{s0}+D_{ss} \le D_{p0} \le D_{p0}+D_p \le 1+D_{ss} \le 1$ $P_{M5}=\frac{Nv_1v_2T}{4L_s}\times\begin{pmatrix}2D_{p0}-2D_{s0}-4D_{ss}+2D_{p0}D_{s0}+\\4D_{p0}D_{ss}+D_p^2-2D_{p0}^2-2D_{ss}^2\end{pmatrix}$	Minimum $P_{n,t}=0$ at $\boldsymbol{D}=\left(0,\frac{1}{2},1,-\frac{1}{2}\right)$ Maximum $P_{n,t}=1$ at $\boldsymbol{D}=\left(0,0,0,-\frac{1}{2}\right)$
Mode 6	Definition domain: $0 \le D_{s0}+D_{ss} \le D_{p0} \le 1+D_{ss} \le D_{p0}+D_p \le 1$ $P_{M6}=\frac{Nv_1v_2T}{4L_s}\times\begin{pmatrix}1-D_{p0}^2+2D_{p0}D_{ss}+2D_{s0}D_{p0}-D_{ss}^2-\\2D_{ss}-D_p-2D_{s0}+D_pD_{s0}\end{pmatrix}$	Minimum $P_{n,t}=0$ at $\boldsymbol{D}=\left(\frac{3}{4},\frac{1}{4},\frac{1}{4},0\right)$ Maximum $P_{n,t}=1$ at $\boldsymbol{D}=(0,0,0,-1)$
Mode 7	Definition domain: $0 \le D_{p0} \le D_{s0}+D_{ss} \le D_{p0}+D_p \le 1+D_{ss} \le 1$ $P_{M7}=\frac{Nv_1v_2T}{4L_s}\times\begin{pmatrix}-D_p^2-2D_pD_{p0}+D_pD_{s0}+2D_pD_{ss}+D_p\\-D_{p0}^2+2D_{p0}D_{ss}+2D_{p0}+D_{s0}^2+2D_{s0}D_{ss}\\-2D_{s0}-D_{ss}^2-4D_{ss}\end{pmatrix}$	Minimum $P_{n,t}=-\frac{1}{4}$ at $\boldsymbol{D}=\left(\frac{1}{2},0,\frac{1}{2},0\right)$ Maximum $P_{n,t}=\frac{1}{2}$ at $\boldsymbol{D}=\left(0,0,\frac{1}{2},-\frac{1}{2}\right)$
Mode 8	Definition domain: $-1+D_{p0}+D_p \le D_{s0}+D_{ss} \le 0 \le D_{p0} \le 1+D_{ss} \le D_{p0}+D_p \le 1$ $P_{M8}=\frac{Nv_1v_2T}{4L_s}\times\left(-D_p^2-D_pD_{p0}-D_pD_{ss}-D_{p0}^2-D_{ss}^2+1\right)$	Minimum $P_{n,t}=0$ at $\boldsymbol{D}=\left(0,0,\frac{1}{2},-1\right)$ Maximum $P_{n,t}=\frac{3}{4}$ at $\boldsymbol{D}=\left(\frac{1}{2},0,\frac{1}{4},-\frac{1}{2}\right)$

REFERENCES

[1] F. Krismer and J. W. Kolar, “Accurate power loss model derivation of a high-current dual active bridge converter for an automotive application,” *IEEE Trans. Ind. Electron.*, vol. 57, no. 3, pp. 881–891, Mar. 2010.

[2] R. M. Burkart and J. W. Kolar, “Comparative η-ρ-σ Pareto optimization of Si and SiC multilevel dual-active-bridge topologies with wide input voltage range,” *IEEE Trans. Power Electron.*, vol. 32, no. 7, pp. 5258–5270, Jul. 2017.

[3] H. Shi, K. Sun, H. Wu, and Y. Li, “A unified state-space modeling method for a phase-shift controlled bidirectional dual-active half-bridge converter,” *IEEE Trans. Power Electron.*, vol. 35, no. 3, pp. 3254–3265, Mar. 2020.

[4] S. Inoue and H. Akagi, “A bidirectional isolated DC-DC converter as a core circuit of the next-generation medium-voltage power conversion system,” *IEEE Trans. Power Electron.*, vol. 22, no. 2, pp. 535–542, Mar. 2007.

[5] B. Zhao, Q. Song, W. Liu, and Y. Sun, “Overview of dual-active-bridge isolated bidirectional DC-DC converter for high-frequency-link power-conversion system,” *IEEE Trans. Power Electron.*, vol. 29, no. 8, pp. 4091–4106, Aug. 2014.

[6] H. Akagi, S. Kinouchi, and Y. Miyazaki, “Bidirectional isolated dual-active-bridge (DAB) DC-DC converters using 1.2-kV 400-A SiC-MOSFET dual modules,” *CPSS Trans. Power Electron. Appl.*, vol. 1, no. 1, pp. 33–40, Dec. 2016, doi: 10.24295/CPSSTPEA.2016.00004.

[7] J. E. Huber, J. Böhler, D. Rothmund, and J. W. Kolar, “Analysis and cell-level experimental verification of a 25 kW all-SiC isolated front end 6.6 kV/400 V AC-DC solid-state transformer,” *CPSS Trans. Power Electron. Appl.*, vol. 2, no. 2, pp. 140–148, 2017, doi: 10.24295/CPSSTPEA.2017.00014.

[8] Z. Guo, Y. Luo, and K. Sun, “Parameter identification of the series inductance in DAB converters,” *IEEE Trans. Power Electron.*, vol. 36, no. 7, pp. 7395–7399, Jul. 2021.

[9] M. N. Kheraluwala, R. W. Gascoigne, D. M. Divan, and E. D. Baumann, “Performance characterization of a high-power dual active bridge DC-to-DC converter,” *IEEE Trans. Ind. Appl.*, vol. 28, no. 6, pp. 1294–1301, Nov./Dec. 1992.

[10] W. Li, S. Zong, F. Liu, H. Yang, X. He, and B. Wu, “Secondary-side phase-shift-controlled ZVS DC/DC converter with wide voltage gain for high input voltage applications,” *IEEE Trans. Power Electron.*, vol. 28, no. 11, pp. 5128–5139, Nov. 2013.

[11] Y. Li, F. Li, F. Zhao, X. You, K. Zhang, and M. Liang, “Hybrid three-level full-bridge isolated buck–boost converter with clamped inductor for wider voltage range application,” *IEEE Trans. Power Electron.*, vol. 34, no. 3, pp. 2923–2937, Mar. 2019.

[12] P. A. M. Bezerra, F. Krismer, R. M. Burkart, and J. W. Kolar, “Bidirectional isolated non-resonant DAB DC-DC converter for ultra-wide input voltage range applications,” in *Proc. Int. Power Electron. Appl. Conf. Expo.*, 2014, pp. 1038–1044.

[13] G. Xu, D. Sha, Y. Xu, and X. Liao, “Hybrid-bridge-based DAB converter with voltage match control for wide voltage conversion gain application,” *IEEE Trans. Power Electron.*, vol. 33, no. 2, pp. 1378–1388, Feb. 2018.

[14] F. Krismer and J. W. Kolar, “Closed form solution for minimum conduction loss modulation of DAB converters,” *IEEE Trans. Power Electron.*, vol. 27, no. 1, pp. 174–188, Jan. 2012.

[15] H. Yu *et al.*, “Globally unified ZVS and quasi-optimal minimum conduction loss modulation of DAB converters,” *IEEE Trans. Transport. Electrific.*, to be published, doi: 10.1109/TTE.2021.3131192.

[16] F. Krismer and J. W. Kolar, “Efficiency-optimized high-current dual active bridge converter for automotive applications,” *IEEE Trans. Ind. Electron.*, vol. 59, no. 7, pp. 2745–2760, Jul. 2012.

[17] G. G. Oggier, G. O. Garcia, and A. R. Oliva, “Modulation strategy to operate the dual active bridge DC-DC converter under soft switching in the whole operating range,” *IEEE Trans. Power Electron.*, vol. 26, no. 4, pp. 1228–1236, Apr. 2011.

[18] G. G. Oggier, G. O. GarcÍa, and A. R. Oliva, “Switching control strategy to minimize dual active bridge converter losses,” *IEEE Trans. Power Electron.*, vol. 24, no. 7, pp. 1826–1838, Jul. 2009.

[19] A. Tong, L. Hang, G. Li, X. Jiang, and S. Gao, “Modeling and analysis of a dual-active-bridge-isolated bidirectional DC/DC converter to minimize RMS current with whole operating range,” *IEEE Trans. Power Electron.*, vol. 33, no. 6, pp. 5302–5316, Jun. 2018.

[20] W. Choi, K.-M. Rho, and B.-H. Cho, "Fundamental duty modulation of dual-active-bridge converter for wide-range operation," *IEEE Trans. Power Electron.*, vol. 31, no. 6, pp. 4048–4064, Jun. 2016.

[21] M. Yaqoob, K. H. Loo, and Y. M. Lai, "A four-degrees-of-freedom modulation strategy for dual-active-bridge series-resonant converter designed for total loss minimization," *IEEE Trans. Power Electron.*, vol. 34, no. 2, pp. 1065–1081, Feb. 2019.

[22] A. Filbà-Martínez, S. Busquets-Monge, and J. Bordonau, "Modulation and capacitor voltage balancing control of a three-level NPC dual-active-bridge DC-DC converter," in *Proc. 39th Annu. Conf. IEEE Ind. Electron. Soc.*, 2013, pp. 6251–6256.

[23] A. Filba-Martinez, S. Busquets-Monge, J. Nicolas-Apruzzese, and J. Bordonau, "Operating principle and performance optimization of a three-level NPC dual-active-bridge DC-DC converter," *IEEE Trans. Ind. Electron.*, vol. 63, no. 2, pp. 678–690, Feb. 2016.

[24] G. Ortiz, H. Uemura, D. Bortis, J. W. Kolar, and O. Apeldoorn, "Modeling of soft-switching losses of IGBTs in high-power high-efficiency dual-active-bridge DC/DC converters," *IEEE Trans. Electron Devices*, vol. 60, no. 2, pp. 587–597, Feb. 2013.

[25] M. A. Moonem and H. Krishnaswami, "Analysis and control of multi-level dual active bridge DC-DC converter," in *Proc. IEEE Energy Convers. Congr. Expo.*, 2012, pp. 1556–1561.

[26] Y. Xuan, X. Yang, W. Chen, T. Liu, and X. Hao, "A novel NPC dual-active-bridge converter with blocking capacitor for energy storage system," *IEEE Trans. Power Electron.*, vol. 34, no. 11, pp. 10635–10649, Nov. 2019.

[27] L. Jin, B. Liu, and S. Duan, "ZVS soft switching operation range analysis of three-level dual-active bridge DC–DC converter under phase shift control strategy," *IEEE Trans. Ind. Appl.*, vol. 55, no. 2, pp. 1963–1972, Mar. 2019.

[28] Z. Deng, G. Wang, K. Wang, and Y. Hao, "Analysis and control of N-level neutral-point clamped dual active bridge DC-DC converter with capacitor voltage balance," in *Proc. Int. Conf. Power Syst. Technol.*, 2018, pp. 2407–2413.

[29] G. E. Sfakianakis, J. Everts, H. Huisman, T. Borrias, C. G. E. Wijnands, and E. A. Lomonova, "Charge-based ZVS modulation of a 3–5 level bidirectional dual active bridge DC-DC converter," in *Proc. IEEE Energy Convers. Congr. Expo.*, 2016, pp. 1–10.

[30] D. Yadeo, P. Chaturvedi, and S. K. Saketi, "A new five level dual active bridge DC-DC converter for solid state transformer," in *Proc. IEEE Int. Conf. Power Electron., Drives Energy Syst.*, 2018, pp. 1–5.

[31] M. A. Moonem, T. Duman, and H. Krishnaswami, "Capacitor voltage balancing in a neutral-point clamped multilevel dc-dc dual active bridge converter," in *Proc. IEEE 8th Int. Symp. Power Electron. Distrib. Gener. Syst.*, 2017, pp. 1–7.

[32] P. Liu, C. Chen, S. Duan, and W. Zhu, "Dual phase-shifted modulation strategy for the three-level dual active bridge DC–DC converter," *IEEE Trans. Ind. Electron.*, vol. 64, no. 10, pp. 7819–7830, Oct. 2017.

[33] P. Liu, C. Chen, and S. Duan, "An optimized modulation strategy for the three-level DAB converter with five control degrees of freedom," *IEEE Trans. Ind. Electron.*, vol. 67, no. 1, pp. 254–264, Jan. 2020.

[34] A. Filba-Martinez, S. Busquets-Monge, and J. Bordonau, "Modulation and capacitor voltage balancing control of multilevel NPC dual-active-bridge DC-DC converters," *IEEE Trans. Ind. Electron.*, vol. 67, no. 4, pp. 2499–2510, Apr. 2020.

[35] P. Jing, C. Wang, W. Jiang, and G. Zhang, "Performance analysis of isolated three-level half-bridge bidirectional DC/DC converter," in *Proc. 7th Int. Power Electron. Motion Control Conf.*, 2012, vol. 3, pp. 1527–1531.

[36] N. H. Baars, J. Everts, C. G. E. Wijnands, and E. A. Lomonova, "Evaluation of a high-power three-phase dual active bridge DC-DC converter with three-level phase-legs," in *Proc. 18th Eur. Conf. Power Electron. Appl. (ECCE Eur.)*, 2016, pp. 1–10.

[37] C. Gammeter, F. Krismer, and J. W. Kolar, "Comprehensive conceptualization, design, and experimental verification of a weight-optimized all-SiC 2 kV/700 V DAB for an airborne wind turbine," *IEEE J. Emerg. Sel. Topics Power Electron.*, vol. 4, no. 2, pp. 638–656, Jun. 2016.

[38] W. Song and B. Lehman, "Dual-bridge DC–DC converter: A new topology characterized with no deadtime operation," *IEEE Trans. Power Electron.*, vol. 19, no. 1, pp. 94–103, Jan. 2004.

[39] Y. Jiao, S. Lu, and F. C. Lee, "Switching performance optimization of a high power high frequency three-level active neutral point clamped phase leg," *IEEE Trans. Power Electron.*, vol. 29, no. 7, pp. 3255–3266, Jul. 2014.

[40] Y. Jiao and F. C. Lee, "New modulation scheme for three-level active neutral-point-clamped converter with loss and stress reduction," *IEEE Trans. Ind. Electron.*, vol. 62, no. 9, pp. 5468–5479, Sep. 2015.

[41] "3.5kW DC/DC PPU series," 2020. [Online]. Available: http://www.fsp-powerland.com/web/upload/2020/09/14/1600061545230330yvq.pdf

[42] Y. Ren, M. Xu, J. Zhou, and F. C. Lee, "Analytical loss model of power MOSFET," *IEEE Trans. Power Electron.*, vol. 21, no. 2, pp. 310–319, Mar. 2006.

[43] F. Krismer, S. Round, and J. W. Kolar, "Performance optimization of a high current dual active bridge with a wide operating voltage range," in *Proc. 37th IEEE Power Electron. Specialists Conf.*, 2006, pp. 1–7.

[44] C. Shao, K. Shen, A. Tong, S. Zhang, Y. He, and L. Hang, "Soft switching method of TPS modulated DAB converters with wide band gap devices," in *Proc. IEEE Appl. Power Electron. Conf. Expo.*, 2019, pp. 1647–1652.

[45] Y. Yan, H. Gui, and H. Bai, "Complete ZVS analysis in dual active bridge," *IEEE Trans. Power Electron.*, vol. 36, no. 2, pp. 1247–1252, Feb. 2021.

[46] Z. He *et al.*, "Modelling and analysis of half-/full-bridge hybrid MMC when riding through DC-side pole-to-ground fault," *High Voltage*, 2021.